이학박사 학위논문

# Two-dimensional Patterns of Umbral Oscillations in Sunspots

## 흑점 암부 진동의 이차원적 양상 연구

2023년 8월

서울대학교 대학원
물리·천문학부 천문학전공
강 주 형

# Two-dimensional Patterns of Umbral Oscillations in Sunspots

## 흑점 암부 진동의 이차원적 양상 연구

지도교수 채 종 철

**이 논문을 이학박사 학위논문으로 제출함**
**2023년 4월**

**서울대학교 대학원**
물리·천문학부 천문학전공
**강 주 형**

**강 주 형의 이학박사 학위논문을 인준함**
**2023년 6월**

위 원 장 ____________________

부 위 원 장 ____________________

위 원 ____________________

위 원 ____________________

위 원 ____________________

# Two-dimensional Patterns of Umbral Oscillations in Sunspots

by

Juhyeong Kang
(kailia@snu.ac.kr)

A dissertation submitted in partial fulfillment of the requirements for
the degree of

**Doctor of Philosophy**

in
Astronomy

in
Astronomy Program
Department of Physics and Astronomy
Seoul National University

Committee:

| | |
|---|---|
| Professor | Yong-Sun Park |
| Professor | Jongchul Chae |
| Professor | Woong-Tae Kim |
| Professor | Gwang-Son Choe |
| Doctor | Eun-Kyung Lim |

# ABSTRACT

Umbral oscillations of intensity and velocity are conspicuous dynamical features in sunspot umbrae. They are associated with slow magnetoacoustic waves propagating upwards from the photosphere to the corona along the magnetic field with the sound speed. Interestingly, recent observational studies have reported that these waves appear to propagate across the magnetic field, forming complex horizontal patterns. The study of oscillation patterns is significant because they give us information about the nature and origin of umbral oscillations and how they can transport their energy from the source region to the chromosphere or above. Moreover, oscillation patterns are useful to infer the properties of the source region because they propagate information about the medium which they pass through. Despite several endeavors to understand the nature of oscillation patterns, it is still elusive. In this thesis, we devised theoretical models to understand the nature of observed patterns in sunspot umbrae using the data obtained from the Fast Imaging Solar Spectrograph of the Goode Solar Telescope and the Atmospheric Imaging Assembly (AIA) of the Solar Dynamics Observatory (SDO).

First, we suggested a theoretical model that interprets the observed spiral-shaped wave patterns (SWPs) as the superposition of the axisymmetric mode and the non-axisymmetric mode of slow waves driven below the sunspot surface in an untwisted magnetic flux tube. We applied the model to the observed SWPs of the line-of-sight (LOS) Doppler velocity. The oscillation period of the SWPs was about 160 s with a duration of about 5 minutes. According to the suggested model, the spiral arm features were reproduced by the non-zero azimuthal modes ($m \neq 0$) driven 1600 km below the surface in the pore. The observed one-armed SWP was formed by the sausage and the kink modes, and the two-armed SWP was reproduced by the sausage and fluting modes in the flux tube.

Second, we analyzed the observational properties of the SWPs by using the SDO/AIA 304 Å. We investigated 496 sunspots in the disk center for 2 hours from the 2013 to 2018 data set. We found 241 SWPs in 140 sunspots with a detection rate of 0.24 per hour; 192 one-armed SWPs, 48 two-armed SWPs, and only one three-armed SWP. The lifetime was 780±250 seconds, and the oscillation period was 149±35 seconds, being comparable to those of conventional umbral oscillations. From the apparent angular speed, we estimated the rotation periods of each SWP. The rotation period of one-armed SWPs is 183±72 seconds, and that of two-armed SWPs is 317±132 seconds. The observational properties of the SWPs were irrespective of the hemisphere, latitude, and size of sunspots. By supposing the observed SWPs originated from localized random events in the interior and by using the eikonal method, we inferred that most of the SWPs were generated between 2 Mm and 10 Mm below the surface with a mean value of about 6 Mm.

Third, we successfully reproduced the temporal evolution of the observed chromospheric oscillation patterns using the subphotospheric fast resonance model. Because of the cutoff wavenumber of the fast body waves, only a few low-order modes can be trapped in the pore-like small-scale flux tube. Through the fast-to-slow mode conversion, the inherited patterns of resonance of fast waves in the subphotosphere can be detected in the chromospheric oscillation patterns of slow waves. This model is the most important achievement of this thesis. It sheds light on the subphotospheric seismology in sunspots in that we can infer the unobservable atmospheric properties from the observed chromospheric oscillation patterns.

Our approaches provide new insights into the nature and origin of umbral oscillations. Furthermore, our results will give a better understanding of the energy transfer of waves from the interior to the solar corona and infer the internal structure below the sunspot surface.

**Keywords:** Sunspots; Magnetohydrodynamics; Solar oscillations; Solar atmosphere;

Solar chromosphere

**Student Number:** 2016-20325

# Contents

# List of Figures

# Chapter 1

# Introduction

Oscillations and waves are ubiquitous dynamic phenomena in the solar atmosphere. One of the most well-known wave phenomena in the Sun is the global standing acoustic waves of pressure mode (*p*-mode) trapped in the solar interior (e.g., Ulrich 1970; Deubner 1975). Since the predominant restoring force of the *p*-mode waves is the gas pressure, they are detected from the temporal changes of the intensity and the Doppler velocity with the dominant period of 5 minutes at the photosphere. The source of these waves has been considered as the turbulent convective disturbance of the photosphere at the top of the convection zone near the solar surface (Goldreich & Kumar 1990). Since the *p*-mode waves are trapped in the spherical Sun, the global patterns of the waves can be mathematically described in terms of spherical harmonics in three dimensions.

In a localized and magnetized region, such as a sunspot, waves have also been reported. The nature of waves in a sunspot is somewhat different from acoustic waves because they are affected by strong magnetic fields. In addition, the waves in a sunspot can transfer their energy from the interior to the corona along the magnetic field and contribute to the heating of the upper atmosphere. Recently their two-dimensional patterns in umbrae have been reported, but it is still elusive what makes these patterns (e.g., Sych & Nakariakov 2014; Zhao et al. 2015). Therefore, the understanding of wave patterns in sunspots is significant in that they give us information about (1) what generates the sunspot waves, (2) how they transfer their energy, and (3) the medium where the waves occur.

## 1.1 Magnetohydrodynamic waves

Magnetohydrodynamics (MHD) is the physics that combines hydrodynamics and electromagnetism to describe the fluid, especially plasma, in a magnetized medium. The importance of the magnetic field relative to the plasma is decided by the *plasma beta*,

$$\beta = \frac{p}{p_m} = \frac{8\pi p}{B^2}, \tag{1.1}$$

where $p$ is the gas pressure and $p_m = B^2/8\pi$ is the magnetic pressure and $\mathbf{B}$ is the magnetic field. This plasma $\beta$ is also represented in the ratio between sound speed ($c_s^2 = \gamma p/\rho$) and Alfvén speed ($v_A^2 = B^2/4\pi\rho$),

$$\beta = \frac{2}{\gamma}\frac{c_s^2}{v_A^2}, \tag{1.2}$$

where $\gamma$ is the specific heat ratio, and $\rho$ is the density of the plasma. In a low-$\beta$ plasma ($\beta \ll 1$), the Lorentz force is dominant, and the Alfvén speed is much higher than the sound speed. In contrast, in a high-$\beta$ region ($\beta \gg 1$), the pressure gradient force is dominant, and the sound speed is much higher than the Alfvén speed.

For the sound waves, the restoring force is the gradient force of the gas pressure. For MHD waves, the Lorentz force also works as the restoring force. This Lorentz force can be separated into the gradient force of the magnetic pressure and the magnetic tension force. The combination of three restoring forces generates several MHD waves.

### 1.1.1 MHD waves in a uniform medium

In a uniform medium, several MHD wave modes are decoupled from each other, so the fundamental properties of each mode can be described easily. Thus it is essential to understand the waves in a uniform medium. In this medium, MHD waves are separated into the *Alfvén waves* (Alfvén 1942) and the *magnetoacoustic waves* depending on the compressibility of the plasma. Figure 1.1 shows the summary of the MHD waves.

#### Alfvén waves

The magnetic tension force generates incompressible waves called Alfvén waves. The Alfvén waves can transfer the magnetic energy only because the restoring force is the magnetic tension force only. The phase speed and group velocity of the Alfvén waves are given by,

$$\frac{\omega}{k} = v_A \cos\theta_B, \tag{1.3}$$

$$\frac{\partial\omega}{\partial\mathbf{k}} = \pm v_A \hat{\mathbf{B}}, \tag{1.4}$$

where $\omega$ is the frequency, $\mathbf{k}$ is the wave vector, $k = |\mathbf{k}|$, $\theta_B$ is the angle between the direction of $\mathbf{k}$ and $\mathbf{B}$, and $\hat{\mathbf{B}} = \mathbf{B}/|\mathbf{B}|$ is a unit vector in direction of $\mathbf{B}$. Thus, the Alfvén waves transport their energy along the magnetic field, and cannot propagate across the magnetic field. The motion of Alfvén waves is perpendicular to both the wave vector and the magnetic field because the Alfvén waves are incompressible ($\mathbf{v} \perp \mathbf{k}$), and the direction of the magnetic tension force is perpendicular to the magnetic field ($\mathbf{v} \perp \mathbf{B}$).

#### Magnetoacoustic waves

The magnetoacoustic waves are the compressible MHD waves generated by the combination of gas pressure and magnetic pressure. From the dispersion relation, the

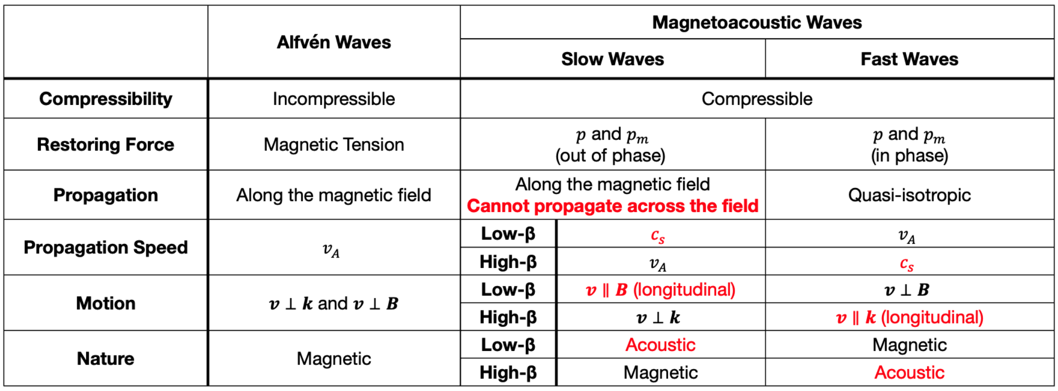

| | **Alfvén Waves** | **Magnetoacoustic Waves** | | |
|---|---|---|---|---|
| | | | **Slow Waves** | **Fast Waves** |
| **Compressibility** | Incompressible | Compressible | | |
| **Restoring Force** | Magnetic Tension | | $p$ and $p_m$<br>(out of phase) | $p$ and $p_m$<br>(in phase) |
| **Propagation** | Along the magnetic field | | Along the magnetic field<br>**Cannot propagate across the field** | Quasi-isotropic |
| **Propagation Speed** | $v_A$ | **Low-β** | $c_s$ | $v_A$ |
| | | **High-β** | $v_A$ | $c_s$ |
| **Motion** | $\boldsymbol{v} \perp \boldsymbol{k}$ and $\boldsymbol{v} \perp \boldsymbol{B}$ | **Low-β** | $\boldsymbol{v} \parallel \boldsymbol{B}$ (longitudinal) | $\boldsymbol{v} \perp \boldsymbol{B}$ |
| | | **High-β** | $\boldsymbol{v} \perp \boldsymbol{k}$ | $\boldsymbol{v} \parallel \boldsymbol{k}$ (longitudinal) |
| **Nature** | Magnetic | **Low-β** | Acoustic | Magnetic |
| | | **High-β** | Magnetic | Acoustic |

Figure 1.1 Summary of the MHD waves.

phase speed of the magnetoacoustic waves is given by,

$$\frac{\omega^2}{k^2} = \frac{1}{2}\left((c_s^2 + v_A^2) \pm \sqrt{(c_s^2 + v_A^2)^2 - 4c_s^2 v_A^2 \cos^2\theta_B}\right). \tag{1.5}$$

The magnetoacoustic waves have two solutions; one is the *fast magnetoacoustic waves* with the positive (+) root, and the other is the *slow magnetoacoustic waves* with the negative (-) root.

Fast magnetoacoustic waves (or fast waves) are generated when two in-phase gradient forces of gas pressure and magnetic pressure disturb the plasma. The phase speed is faster than two characteristic speeds (sound speed and Alfvén speed) and propagates quasi-isotropically in the low-$\beta$ and the high-$\beta$ plasma. The velocity perturbation is in the plane of the wave vector and the magnetic field, and the field-parallel component is in phase with the perpendicular component. In the high-$\beta$ region, the fast waves have an acoustic nature transporting more acoustic energy than magnetic energy with the phase speed of the sound speed. In addition, they are longitudinal because the velocity perturbation is aligned with the wave vector. On the other hand, in the low-$\beta$ plasma, the fast waves transfer magnetic energy with the Alfvén speed, and the motion is perpendicular to the magnetic field. Thus (magnetic) fast waves in the low-$\beta$ region are sometimes called *compressible Alfvén waves.*

Slow magnetoacoustic waves (or slow waves) are disturbed by two out-of-phase gradient forces of gas pressure and magnetic pressure. The phase speed is slower than the sound speed and the Alfvén speed. Similar to the Alfvén waves, they propagate along the magnetic field and cannot propagate across the field line. As with the fast waves, the velocity perturbation lies in the same plane of the wave vector and the magnetic field, but the field-parallel component is out of phase with the perpendicular component. In fact, the motion of the slow waves is orthogonal to the motion of fast waves. In the high-$\beta$ region, the slow waves have magnetic nature transporting magnetic energy, and they are transverse to the wave vector. In the low-

$\beta$ region, the slow waves are considered one-dimensional sound waves because they propagate along the magnetic field, and their motion is aligned with the magnetic field showing the longitudinal nature. See more details in Roberts (2019).

### 1.1.2 Waves in a flux tube

Except for the ideal case, plasma in the Sun is non-uniform and inhomogeneous because of the structured magnetic field and the effect of gravity. In an inhomogeneous medium, waves are dispersive: the propagation speed depends on the wavelength. Thus we should understand the properties of the waves in such a medium.

At first, we consider the magnetoacoustic waves in a cylindrical magnetic flux tube surrounded by a uniform medium. If the waves are trapped in the flux tube and exponentially decay in the surroundings, the waves in the flux tube can be classified as *surface waves* or *body waves* by the behavior of the wave motions (see Figure 1.2). The surface waves exponentially decay from the interface, so the radial motion is maximum at the interface. The motion of body waves also decays outside the flux tube but is oscillatory within the flux tube. The total pressure perturbation ($p_T$) of waves inside the tube can be described by Bessel functions $I_m$ and $J_m$ in cylindrical coordinates $(r, \theta, z)$,

$$p_T \propto \left\{ \begin{matrix} I_m(k_r r) \exp i(k_z z + m\theta - \omega t), & \text{Surface waves} \\ J_m(k_r r) \exp i(k_z z + m\theta - \omega t), & \text{Body waves} \end{matrix} \right\} (r < R) \tag{1.6}$$

where $m$ is the azimuthal mode, $k_r$ is the effective radial wavenumber, $k_z$ is the vertical wavenumber. The total pressure perturbation in the exterior is described by the Bessel function $K_m$.

The waves in the flux tube can also be classified according to the distinctive geometric patterns of the boundary (see Figure 1.3). The symmetric expanding or contracting boundary is referred to as *sausage mode waves.* The central axis of the

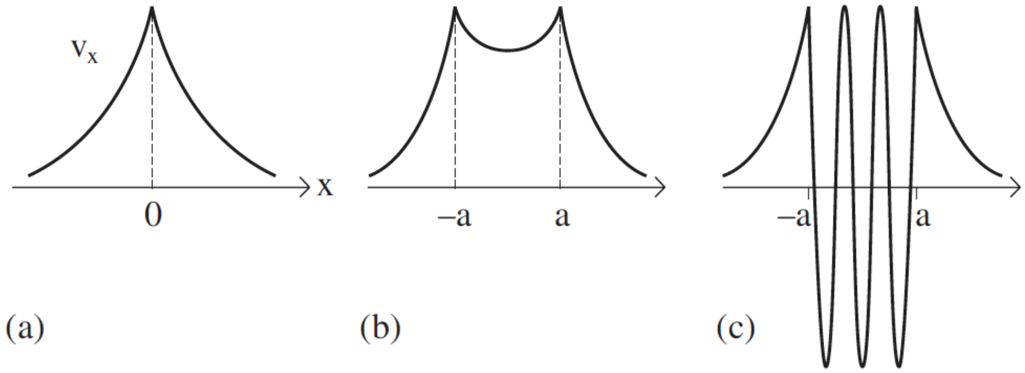

Figure 1.2 A surface wave on (a) a single magnetic interface, (b) a magnetic flux tube, (c) and a body wave on a magnetic flux tube. The surface waves decay away from the boundary where the velocity is maximized. In contrast, the body waves are oscillatory in the flux tube. (From Priest (2014))

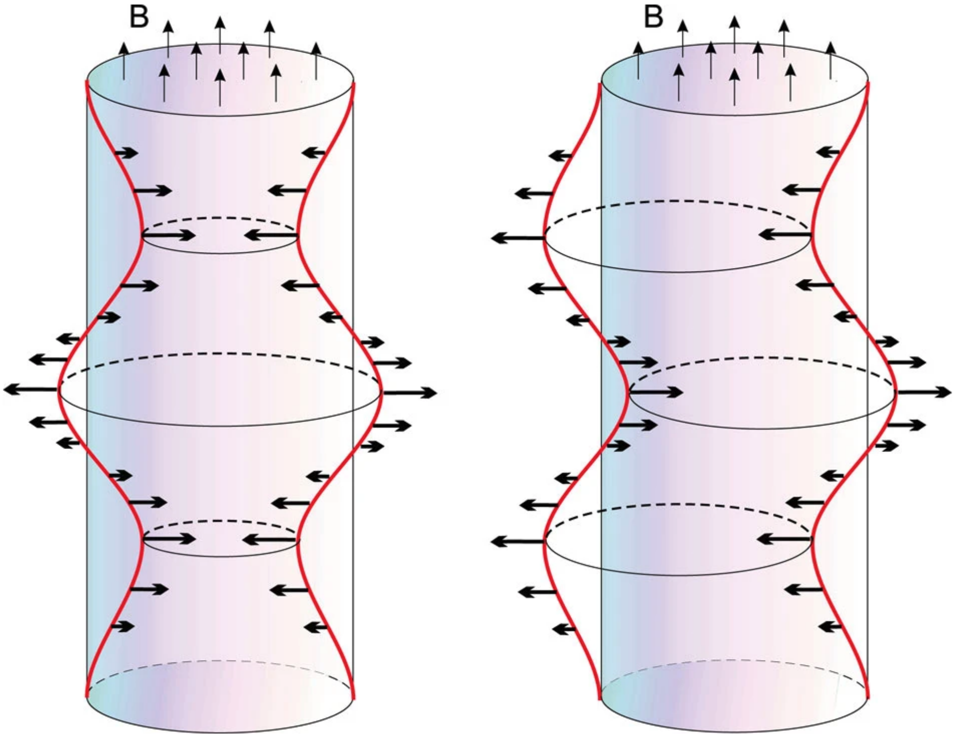

Figure 1.3 A sausage mode wave (left) and a kink mode wave (right) on the magnetic flux tube. The sausage wave has the symmetric motion of the flux tube. The kink wave is described by the asymmetric motion displacing the central axis of the flux tube.(From Morton et al. (2012))

tube is not perturbed because of the symmetric motion. In contrast, asymmetric transverse motions disturb the central axis of the (thin) flux tube like the motion of a snake. These waves are called the *kink mode waves*. Moreover, the more complex higher-order motion of the tube boundary is called *fluting modes*. The motions of kink and fluting modes can be linearly or circularly polarized (See the review Nakariakov et al. 2021). More generally, symmetrical motions of either surface or body waves are categorized as sausage waves, and asymmetric motions are classified as kink waves.

### 1.1.3 Waves in gravitationally stratified atmosphere

When the gravity force is not negligible, we have to consider the effect of gravity on the medium. In this medium, the mass density and the plasma pressure exponentially decrease with height: $\rho = \rho_0 \exp(-z/H_0)$ and $p = p_0 \exp(-z/H_0)$, where $H_0 = c_s^2/\gamma g$ is the density scale height, and $g$ is the gravitational acceleration. On the other hand, the amplitude of the oscillations becomes large with height because of the energy conservation ($v \propto \rho^{-1/2} \propto \exp(z/2H_0)$). This atmosphere is called the *gravitationally stratified medium.*

Two distinctive effects occur in a gravitationally stratified medium: the *acoustic cutoff frequency* and the *mode conversion.*

#### Acoustic cutoff frequency

The acoustic cutoff frequency is the critical frequency of whether a particular frequency of acoustic waves can propagate. The acoustic cutoff frequency acts as a high-frequency filter that the waves with the frequency below this cannot propagate upwards but exponentially decay, which are called *evanescent waves* (Kalkofen et al. 1994; Chae & Goode 2015). Only the waves above the acoustic cutoff frequency can pass through the medium.

This acoustic cutoff frequency occurs due to the presence of a gravitational force acting as a buoyancy force. The density gradient creates the buoyancy force opposing the propagation direction of waves. This buoyancy force is proportional to the distance from the equilibrium position in the stratified medium. When the buoyancy force is stronger than the pressure gradient force, waves cannot propagate. It means that the waves with a wavelength ($\lambda$) longer than the given length scale $2H_0$ cannot propagate. From the relation of $\omega = c_s k \propto \lambda^{-1}$, this critical length can be converted to the timescale of cutoff frequency $\omega_c$,

$$\omega_c = \frac{c_s}{2H_0} = \frac{\gamma g}{2c_s}. \tag{1.7}$$

Therefore, the acoustic waves of frequency larger than the acoustic cutoff frequency can propagate.

Note, the acoustic cutoff frequency has a similar value to the Brunt-Väisälä frequency ($N$) of the internal gravity waves at the temperature-minimum region. If the waves propagate obliquely, the acoustic waves with a frequency higher than the acoustic cutoff and the internal gravity waves with a frequency lower than the Brunt-Väisälä frequency can propagate. Thus the acoustic cutoff acts as a high-pass filter of the acoustic waves, but the Brunt-Väisälä frequency performs as a low-pass filter of the internal gravity waves. For the case of slow (acoustic) MHD waves in the low-beta region, the internal gravity waves cannot propagate because the waves are aligned with the magnetic field ($k_z \gg k_\perp$). The dispersion relation of the acoustic-gravity waves is given by (Roberts 2019),

$$k_z^2 = \frac{\omega^2 - \omega_c^2}{c_s^2} + k_\perp^2 \left( \frac{N^2}{\omega^2} - 1 \right). \tag{1.8}$$

See more details in chapter 9 of Roberts (2019).

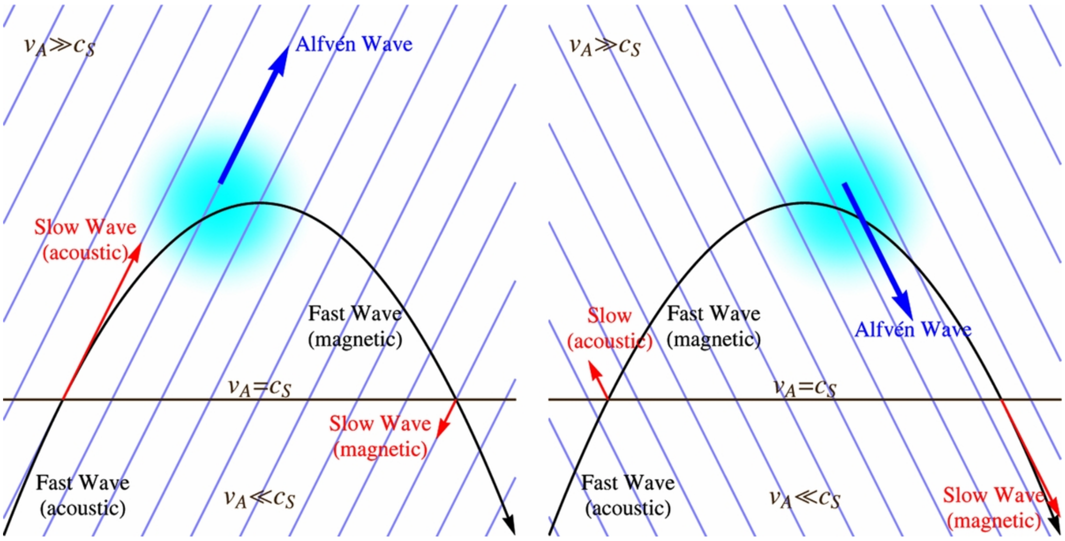

Figure 1.4 Schematic diagram illustrating the mode conversion in two inclined magnetic fields (sky blue). Here the curved black arrow indicates the ray path of the fast MHD waves, the red arrow represents the wave vector of the slow waves, and the blue arrow is the wave vector of the Alfvén waves. Some fast (acoustic) waves are converted to slow (acoustic) waves in the equipartition layer (black solid line), and some fast (magnetic) waves are converted to Alfvén waves. The efficiency of the mode conversion decrease with the angle between the wavevector and the magnetic field. (From Khomenko & Cally (2012))

### Mode conversion

In an inhomogeneous medium, some of the energy of one wave mode can be transferred to other wave modes. Assume that the atmosphere is gravitationally stratified, but temperature and the magnetic field strength are not varying with height. In this atmosphere, the sound speed is constant because it depends on the temperature ($c_s \propto T$), but the Alfvén speed is exponentially increased because it is inversely proportional to plasma density ($v_A \propto \rho^{-1/2} \propto \exp(z/2H_0)$). Thus the sound speed is higher than the Alfvén speed in the deep region (high-$\beta$), while the sound speed is lower than the Alfvén speed in the high atmosphere (low-$\beta$). In between, there is a region where the sound speed and the Alfvén speed are about the same, called the equipartition layer. In this layer, the speeds of slow and fast waves become similar, and the two modes are coupled. Thus the energy can be converted between two modes, and this process is the fast-to-slow *mode conversion.* This mode conversion process conserves the nature of the waves. It means that the **acoustic** nature of fast waves in the high-$\beta$ region are conserved when they are converted to **(acoustic)** slow waves, or vice versa (Figure 1.4).

In this thesis, we do not add the gravity force on the momentum equation for simplification but utilize the concept of the acoustic cutoff frequency and the fast-to-slow mode conversion process to interpret observed features.

## 1.2 Umbral oscillations in sunspots

A sunspot is a dark region where the magnetic fields are concentrated. As the magnetic tension suppresses the convective flow, the sunspot looks darker, with a temperature of 4000 K. The sunspot can be separated into the umbra and penumbra. The umbra has strong vertical magnetic fields that suppress heat transport, so it is cooler than its surroundings. The penumbra surrounds the umbra with the inclined magnetic fields, and the field strength is weaker than the umbra. The penumbra is brighter than the umbra because the magneto-convective cell that transfers the internal heat to the surface along the magnetic fields becomes larger in a weaker and more inclined magnetic fields. Especially a sunspot without the penumbra is called a *pore*.

One of the most prominent physical phenomena in sunspots is umbral oscillations of intensity and Doppler line-of-sight (LOS) velocity (Figure 1.5). The first detection of intensity oscillations in the chromosphere of sunspot umbrae was reported by Beckers & Tallant (1969) using the Ca II H and K lines. After the first detection, the umbral oscillations were also found in the photosphere (Bhatnagar et al. 1972; Lites 1984), the transition region, and the corona (Gurman et al. 1982; O'Shea et al. 2002; Tian et al. 2014). The oscillation period of the umbral oscillation is around 5 minutes in the photosphere, 2-3 minutes above the chromosphere (Figure 1.6).

The nature of umbral oscillations has been known as slow magnetoacoustic waves. They are compressible waves because they display the fluctuation of either intensity or LOS velocity. Moreover, they propagate upwards along the magnetic field from the photosphere to the chromosphere and above (Lites 1984; Centeno et al. 2006; Felipe et al. 2010). Their propagation speed is around the local sound speed. The 3-minute period above the chromosphere comes from the acoustic cutoff frequency at the temperature-minimum region of 2-3 minutes (Kalkofen et al. 1994). The long-period waves of larger than 2-3 minutes are reflected at the temperature-minimum region, but waves shorter than the acoustic cutoff period can propagate above the temperature-minimum region. Actually, considering a temperature gradient and radiative heating and cooling, a portion of 5-minute waves can propagate upwards (Mihalas & Mihalas 1984; Bunte & Bogdan 1994; Chae & Litvinenko 2018; Chae et al. 2023). Therefore, observed umbral oscillations are interpreted as slow MHD waves.

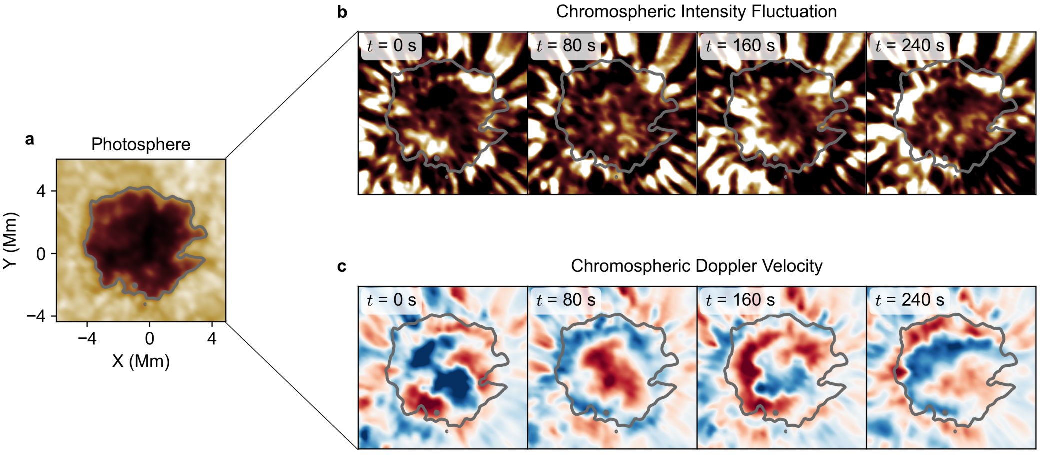

Figure 1.5 Chromospheric umbral oscillations. **a** is the intensity image at the photosphere obtained from the GST/FISS continuum on June 3rd, 2014, at 17:45:47 UT. **b** is the time series of the chromospheric intensity fluctuation observed from the H$\alpha$ line core from 17:44:27 UT to 17:49:47 UT. **c** is the time series of the chromospheric Doppler LOS velocity measured from the H$\alpha$ line profile. Gray contours in all panels show the boundary of the pore.

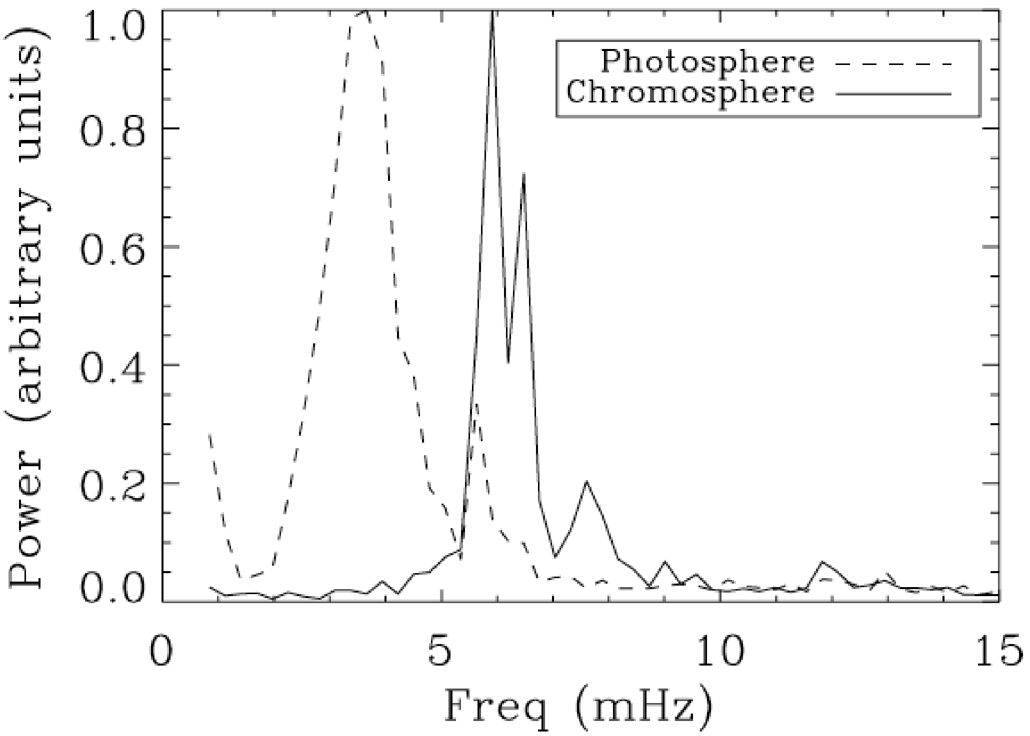

Figure 1.6 Average power spectrum for a sunspot umbra. The power spectrum derived from the photospheric line is maximized at a frequency of 3.3 mHz, and the power spectrum obtained from the chromospheric line is peaked at a frequency of 6 mHz. (From Centeno et al. (2006))

There are two plausible excitation sources of umbral oscillations; one is the external $p$-mode, and the other is the internal magneto-convection. In the external driving model, the umbral oscillations are generated by the incoming $p$-mode waves from the quiet sun region. A portion of the energy of incident waves can be absorbed by the sunspot (e.g., Cally et al. 1994; Cally & Bogdan 1997; Cally et al. 2003). This idea has been supported by measuring the absorption of surrounding $p$-mode waves (Zhao & Chou 2013; Grant et al. 2022). In contrast, the internal excitation model suggests that the umbral waves are disturbed by a local magneto-convection inside a sunspot (e.g., Lee 1993; Jacoutot et al. 2008). Several works have supported this model by measuring enhanced wave energy above umbral dots and light bridge of magneto-convection (Jess et al. 2012; Chae et al. 2017; Cho et al. 2019).

Interestingly, recent observational works have reported that the umbral waves seem to propagate across the magnetic fields, forming two-dimensional patterns (Figure 1.7). Sych & Nakariakov (2014) first reported the spiral-shaped wave patterns observed in the temperature-minimum region and the corona. Zhao et al. (2015) identified the fast-moving ring-like patterns that appear to propagate across the magnetic fields with the speed of about 40 km $s^{-1}$ near the photosphere, and this speed is much faster than the sound speed of less than 10 km $s^{-1}$. They interpreted these patterns as slow magnetoacoustic waves by measuring intensity fluctuation and vertical propagation speed. However, it is still elusive what makes two-dimensional patterns of umbral oscillations even though the slow waves cannot propagate across the magnetic field. Here, we suggest two models that can reproduce the observed chromospheric patterns of umbral oscillations and analyze these to derive their nature and origin.

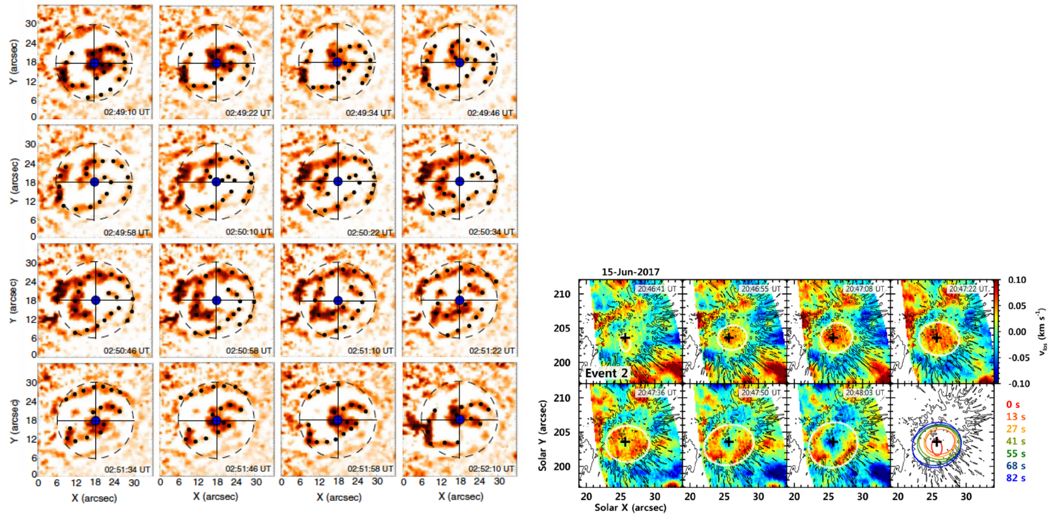

Figure 1.7 Two-dimensional patterns of umbral oscillations. Time series of spiral-shaped umbral oscillations observed on December 08th, 2010, with the SDO/AIA 304 Å line (left). Time series of ring-like patterns of umbral oscillations obtained with the GST/FISS Fe I 5434 Å line on June 15th, 2017 (right). Image reproduce from Sych & Nakariakov (2014) (left) and from Cho et al. (2019) (right).

## 1.3 Importance of the oscillation patterns

Numerous studies have successfully interpreted umbral oscillations in one dimension. However, this one-dimensional perspective cannot explain why the umbral oscillation has two-dimensional patterns. Thus, the new physical interpretation is indispensable to comprehend the nature of umbral oscillations.

Moreover, the umbral oscillations patterns may give us the atmospheric condition of their origin. The waves have the information of the medium that they pass through. Thus, if we understand wave propagation and nature, we can derive the properties of the unobservable atmosphere, such as plasma density, temperature, and magnetic strength, like the helioseismology of $p$-mode or the seismology of the earthquake.

One of the unsolved problems in solar physics is the coronal heating. MHD waves in sunspots can contribute to the heating of the upper atmosphere because they can transfer either kinetic or magnetic energy. Therefore if we understand how they transport their energy from the solar interior to the corona, we can give a clue to the coronal heating problem.

## 1.4 Instruments

In order to analyze two-dimensional patterns of umbral oscillation, we need data satisfying several requirements. First, spectral data is preferable. Doppler velocity is only affected by the motion of the plasma, but the intensity can be affected by the plasma density and temperature as well as the plasma motion. Thus, the Doppler velocity is fundamental to derive the properties of the waves. Second, the field of view (FOV) should be larger than 10 Mm. The size of patterns of umbral oscillations is comparable to the size of the umbrae, so the data should cover the size of the umbrae or pore. Third, the spatial resolution should be better than 0.5 Mm.

In order to resolve the structures of the two-dimensional patterns and to accurately derive the apparent radial propagation speed of them in a radial direction, we need a high-spatial resolution of more than one-third of the radius of the umbrae. Finally, the temporal resolution (time cadence) should be shorter than 30 seconds. To observe the temporal evolution of the patterns and measure the radial speed in the umbrae, high-temporal resolution is required. In this thesis, therefore, we examined the data taken from the Fast Imaging Solar Spectrograph (FISS; Chae et al. 2013b) of 1.6 m Goode Solar Telescope (GST; Cao et al. 2010) that satisfy the requirements.

The FISS is optimized to study magnetohydrodynamic phenomena from the photosphere to the chromosphere (Figure 1.8). This instrument simultaneously observes two chromospheric line profiles of H$\alpha$ and Ca II 8542 Å band covering 10 Å and 13 Å, respectively. The FISS generates the three-dimensional data $(\lambda, y, x)$ at one scanning, where $\lambda$ is the wavelength, $x$ is the scanning position, and $y$ is the slit position. The spectral resolution is about 0.019 Å for H$\alpha$ band and is about 0.026 Å for Ca II 8542 Å band. The spatial resolution is $0.16'' \times 0.16''$, and the temporal cadence for $21'' \times 41''$ is 20 seconds. See details in Chae et al. (2013b).

We also used the data of the Atmospheric Imaging Assembly of the Solar Dynamics Observatory (SDO/AIA; Lemen et al. 2012) for statistical analysis of spiral-shaped wave patterns. The AIA observes the full-disk image of the Sun from the temperature-minimum to the corona using two ultraviolet channels (1600 Å, 1700 Å) and seven extreme ultraviolet bands (94 Å, 131 Å, 171 Å, 193 Å, 211 Å, 304 Å, 335 Å) with the spatial resolution of $0.6''$ and the temporal cadence of 12 seconds. See details in Lemen et al. (2012).

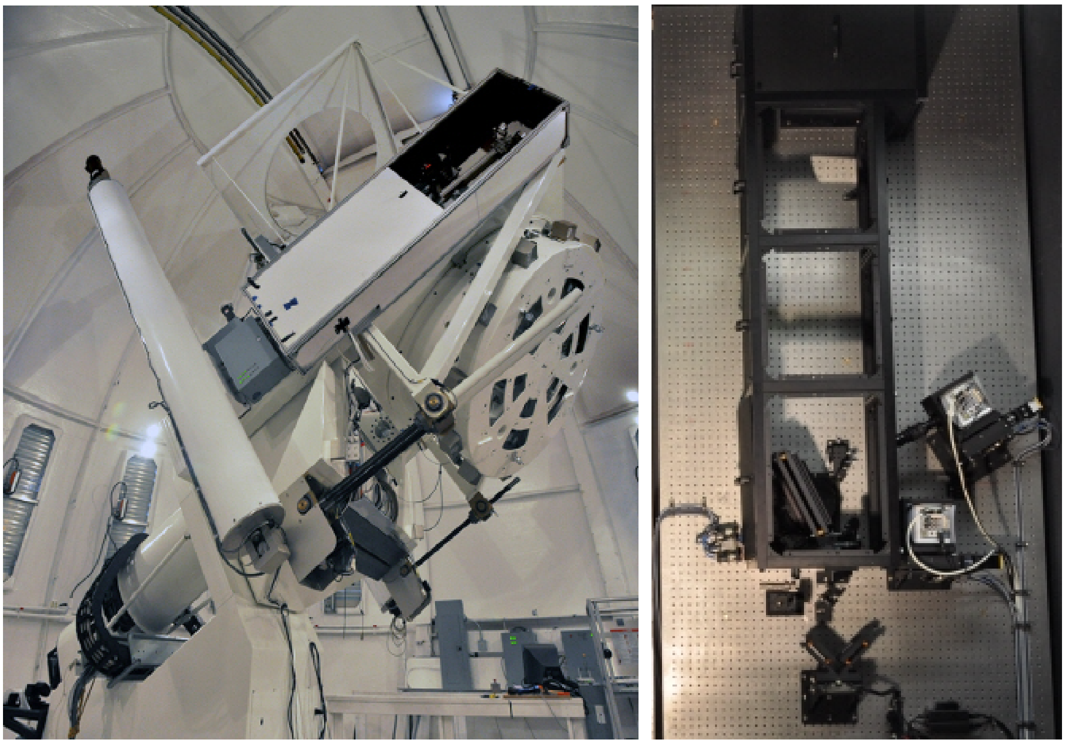

Figure 1.8 (Left) The Goode Solar Telescope (GST) and (right) the Fast Imaging Solar Spectrograph (FISS). (From http://fiss.snu.ac.kr/instrument)

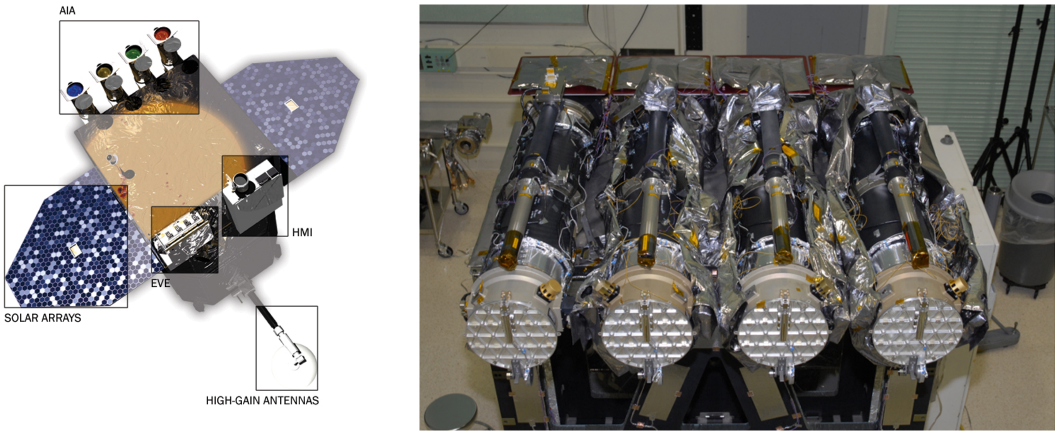

Figure 1.9 (Left) Solar Dynamics Observatory (SDO) and (right) the Atmospheric Imaging Assembly (AIA). (From https://sdo.gsfc.nasa.gov)

## 1.5 Outline

This thesis consists of several pieces of my work on the nature of the two-dimensional patterns of the umbral oscillations. It may appear to the readers that the individual works in the thesis are not well-organized, even lacking consistency. This is because they reflect the trial and error I experienced throughout my academic journey. They also display the history of my growth in understanding this interesting topic. I believe the early works are meaningful themselves, but the final research is more significant because it is based on my most recent understanding.

In Chapter 2, we suggest the internal excitation model (IEM) that can explain the spiral-shaped wave patterns. In Chapter 3, we analyze the statistical properties of the SWPs obtained from the SDO/AIA 304 Å line based on the internal excitation model. In Chapter 4, we propose another model of the subphotospheric fast resonance wave model that can reproduce the chromospheric umbral oscillations more precisely. In this chapter, we correct a mistake in the equation in the IEM and explain the frequency-dependent patterns of umbral oscillations that cannot be described in the IEM. In Chapter 5, we provide the summary and conclusion of our findings, and then we suggest ideas for future works.

# Chapter 2

# The Physical Nature of Spiral Wave Patterns in Sunspots[1]

## 2.1 Introduction

Wave motions are a conspicuous dynamic phenomenon observed in sunspots. The first detection of sunspot waves in the chromosphere was reported by Beckers & Tallant (1969). Subsequent works revealed that the predominant period of the waves is 5 minutes in the umbral photosphere (Bhatnagar et al. 1972), and 3 minutes in the chromosphere (Beckers & Schultz 1972). Sunspot waves were also observed in the transition region and corona with the periods of less than three minutes (e.g. De Moortel et al. 2002; Sych et al. 2009; Tian et al. 2014). Furthermore, a radially propagating wave pattern was detected in the sunspot penumbra that is known as running penumbral waves (RPWs; Giovanelli 1972; Zirin & Stein 1972). A comprehensive review of sunspot waves can be found in Khomenko & Collados

---

[1] Most of the contents in this chapter were written as a separate paper: Juhyung Kang, Jongchul Chae, Valery M. Nakariakov, Kyuhyoun Cho, Hannah Kwak, and Kyeore Lee, *"The physical Nature of Spiral Wave Patterns in Sunspots"*, 2019, ApJL, 877, 9

(2015).

The nature of 3 minute chromospheric oscillations has been attributed to upward propagating slow magnetoacoustic waves (Lites 1984; Centeno et al. 2006). Centeno et al. (2006) clearly showed the propagating property of the waves by measuring the phase difference between the time series of the line-of-sight (LOS) velocity in the photosphere and that in the chromosphere. In the same context, the RPWs have been interpreted as the slow waves propagating along the inclined magnetic field lines (Bloomfield et al. 2007; Löhner-Böttcher & Bello González 2015).

The plausible driving sources of sunspot waves are external $p$-modes and internal magnetoconvection. The external driving scenario assumes that $f$- and $p$-mode waves in a quiet Sun propagate into a sunspot. A fraction of the energy of the incident $f$- and $p$-mode is absorbed by its conversion into a slow magnetoacoustic mode at the plasma-$\beta$ equal to one layer (e.g., Cally et al. 1994; Cally & Bogdan 1997; Cally et al. 2003). Zhao & Chou (2013) successfully observed the absorption of the $f$- and $p$-mode wave energy in a sunspot in the $k - \omega$ diagram. In the internal driving model, magnetoconvection occurring inside a sunspot can excite the waves. The radiative magnetohydrodynamics simulations of the magnetoconvection showed that multi-frequency waves can be generated in a magnetic concentration region such as a sunspot (Jacoutot et al. 2008). Chae et al. (2017) found that the wave energy flux was enhanced around the light bridge and umbral dots, and they concluded that the magnetoconvection may be the driving source of 3 minute oscillations. The internal excitation was further supported by Cho et al. (2019)'s identification of several patterns characterized by oscillation centers and radial propagation above individual umbral dots that are under substantial changes. Recent works suggested that an internal driving source may be located, below the sunspot photosphere down to 5 Mm in the sunspot's flux tube, by analyzing the photospheric fast-moving wave patterns (Zhao et al. 2015; Felipe & Khomenko 2017).

Interestingly, recent observational works reported that in the horizontal plane, 3 minute oscillations often appear in sunspot umbrae as one- and two-armed spiral wave patterns (SWPs; Sych & Nakariakov 2014; Su et al. 2016; Felipe et al. 2019). SWPs apparently propagate radially out at the velocity of around 20 km $s^{-1}$, and also propagate upward (Su et al. 2016). Because these propagating properties are similar to RPWs, Su et al. (2016) concluded that observed SWPs could be associated with the slow waves propagating along a twisted magnetic field. Sych & Nakariakov (2014), however, pointed out that the magnetic field should be uniformly twisted in low-$\beta$ plasma of sunspots, and it cannot contribute to the non-uniformity of a SWP. Moreover, the observed SWPs highlight the structure of the wavefront in a certain horizontal cross section of the magnetic flux tube, which does not require the flux tube twisting. Very recently, Felipe et al. (2019) also concluded that although the twist can affect the shape of the observed SWPs, it is not their main cause.

In this chapter we present a simple model that SWPs can naturally appear in an untwisted magnetic flux tube when non-axisymmetric disturbances from below the surface are taken into account. We observationally identify one- and two-armed SWPs in a pore in Doppler velocity maps of the H$\alpha$ line profiles, and develop a theoretical model explaining the appearance of SWPs. In section 2.2, we describe the observations, and summarize observational results. In section 2.3 we describe the theoretical model that reproduces the SWPs, together with their simulation. Finally, in Section 2.4 we discuss and conclude the main results.

## 2.2 Observation

We observed a pore in NOAA 12078 on 2014 June 3 from 16:48:41 to 17:56:32 UT with the 1.6 m Goode Solar Telescope. The target was located at $x = 160''$, $y = -300''$ when we started the observation. In this chapter, we used the data acquired by the Fast Imaging Solar Spectrograph (FISS) in the H$\alpha$ band, and this is the same data analyzed previously in Chae et al. (2015). The FISS scanned the pore with a spectral sampling of 0.019 Åand spatial sampling of 0.″16, covering a field of view of 20″ by 40″. The exposure time was 30 ms, and the time cadence of the data was 20 s. The basic calibration was performed as described by Chae et al. (2013b). We measured the LOS Doppler velocities for all data pixels by using the lambdameter method (Chae et al. 2013a) with the lambdameter chord of 0.4 Å. To highlight 3 minute oscillations, we filtered the data in frequency, leaving only the frequencies of 5.5 – 9 mHz.

From the filtered Doppler velocity maps, we identified three SWPs, but here we deal only with the the case studies of one- and two-armed SWPs. The left panels of Figure 2.1 show the one- and two-armed SWPs measured from the velocity maps at 17:18:20 UT and 17:44:47 UT, respectively. The temporal evolution of these patterns during one cycle is illustrated in Figure 2.4 and Figure 2.5. These wave patterns rotated in the counterclockwise direction. The spiral arm structures are seen to move outward, and their amplitude become to zero near the boundary of the pore. On the other hand, the center of the arms moved abruptly inward direction while rotating, like a spiral; hereafter, we call this as *spiraling*. We determined the duration of the SWPs by the visual inspection of the rotating motion. It was found to be about 4 minutes for the one-armed spiral, and 5 minutes for the two-armed spiral. From the wavelet analysis, we estimated the oscillation period of SWPs at about 120 s at the center of the pore and at about 250 s near its boundary. The period averaged over the pore is about 165 s.

To identify the spatial fluctuations of the patterns in the azimuthal direction, the discrete Fourier transform was applied along the dashed line. The Figure 2.1 shows the time-averaged azimuthal power spectra of the two SWPs constructed along the two circles marked by the dashed curves. At these two radii, the power of non-zero azimuthal mode $m$ is the largest. In the case of the one-armed SWP, most of the

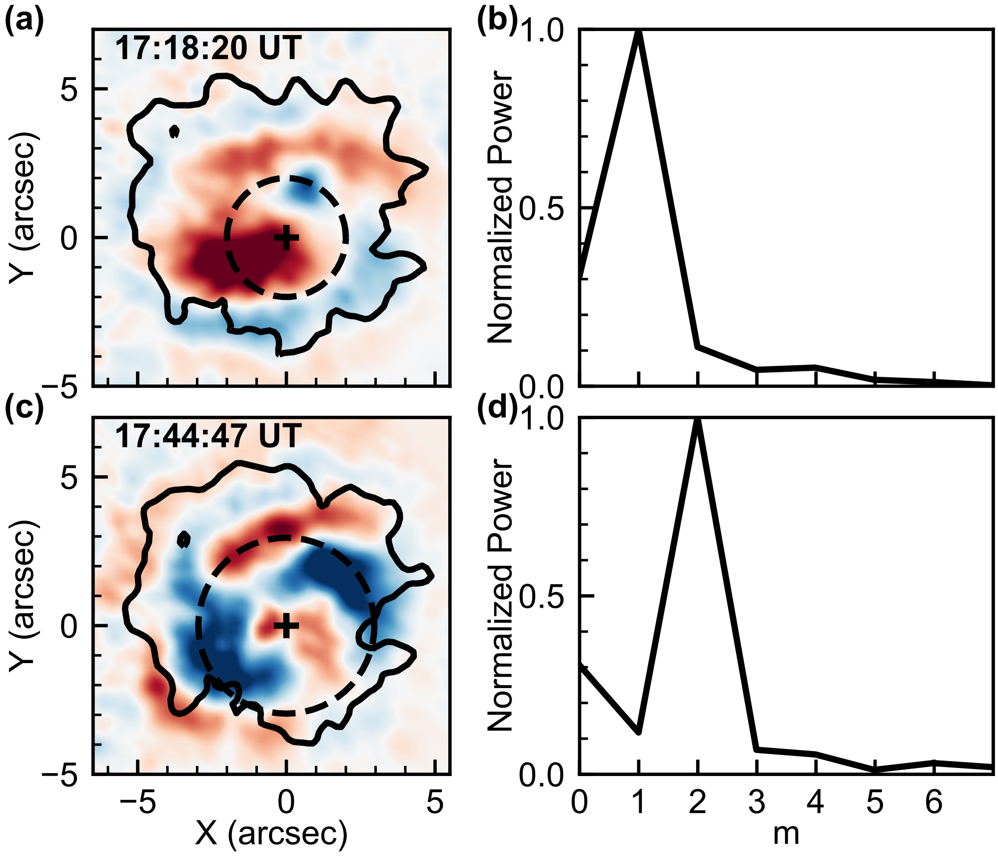

Figure 2.1 Snapshots of the LOS Doppler velocity maps (left panels), and their time-averaged azimuthal power spectra in the azimuthal direction along the dashed line (right panels). Blue (red) color represents upflows (downflows), and the saturation amplitude of velocity is 3 km s$^{-1}$. The black contour represents the boundary of the pore. The cross symbol indicates the center of the dashed line, and this position is set to be the origin. The radius of the dashed line is $2''$ for the one-armed SWP (a) and $3''$ for the two-armed SWP (c).

power is concentrated at $m = 0$ and $m = 1$ (panel (b)). For the two-armed spiral, the power is concentrated at the $m = 0$ and $m = 2$ (panel (d)). These indicate that the SWPs are composed of at least two azimuthal modes. We found that during each event, both the azimuthally symmetric modes ($m = 0$) and the non-symmetric mode ($m = 1$ or 2) appeared and disappeared together. The power of $m = 0$ mode at the chosen radius fluctuated substantially for the period of about 80 s, whereas the power of $m = 1$ or 2 mode changed slowly with time.

We detected such SWPs in other sunspots as well. Roughly speaking, from an one hour observation, two or three SWPs occurred inside each sunspot. The rotation direction of the SWPs did not have any hemispheric dependence. In some cases, in fact, two SWPs of opposite rotation directions were observed in the same sunspot at two different times. Even though such SWPs were detected in any types of sunspots, the spiral arms were simply shaped in small axisymmetric sunspots. The details of these observational results will be described in a subsequent paper.

## 2.3 Modeling

To interpret the detected SWPs, we first consider azimuthal wave modes in an untwisted uniform thick magnetic cylinder with the magnetic field along the $z$ direction, following Edwin & Roberts (1983). The observed pore is well compatible with this assumption because it contains a straight field that is confined to the pore's boundary. The internally oscillatory solution (body waves) of the transverse and longitudinal velocity components in cylindrical coordinates $(r, \theta, z)$ are given as follows (Spruit 1982; López Ariste et al. 2016):

$$v_r = -\frac{\omega^2 - k_z^2 c_s^2}{\omega^2 n} A_m J'_m(k_r r) \exp i\,(k_z z + m\theta - \omega t), \tag{2.1}$$

$$v_z = -i\frac{k_z c_s^2}{\omega^2} A_m J_m(k_r r) \exp i\,(k_z z + m\theta - \omega t), \tag{2.2}$$

where $k_z$ is the wavenumber along the field, $\omega$ is the frequency, $c_s$ is the sound speed, $A_m$ is the amplitude of an azimuthal mode $m$, $J_m$ is the Bessel function of the first kind, and $J'_m$ is its derivative. In this chapter, we follow the general naming convention for the integer azimuthal modes: *sausage* mode for $m = 0$, *kink* mode for $m = 1$, and *fluting* modes for $m \geq 2$.

The effective radial wavenumber $k_r$ is given by (Edwin & Roberts 1983)

$$k_r^2 = \frac{\left(\omega^2 - c_s^2 k_z^2\right)\left(\omega^2 - c_A^2 k_z^2\right)}{\left(c_s^2 + c_A^2\right)\left(\omega^2 - c_T^2 k_z^2\right)}, \tag{2.3}$$

where $c_A$ is the Alfvén speed, and $c_T$ is the tube speed, $c_T^2 = c_s^2 c_A^2/(c_s^2 + c_A^2)$. For body waves $n^2$ must be positive, and for slow modes the phase speed $\omega/k$ lies between the tube speed and sound speed (Roberts 2006).

In addition, we assume that the driving source of the wave is located below the photosphere inside the flux tube. This approach is in line with the suggestion of Zhao et al. (2015) and Felipe & Khomenko (2017) made to interpret the photospheric fast-moving radial wave patterns. In this scenario a fast mode wave is driven at the high-$\beta$ region, then it propagates quasi-isotropically to the $\beta = 1$ layer (see Figure 2.2). Thus, the arrival time $t_A(r)$ at the $\beta = 1$ layer is given as a function of the transverse distance $r$ from the center of the source,

$$t_A(r) = \frac{\sqrt{r^2 + d^2}}{v_{\text{fast}}}, \tag{2.4}$$

where $d$ is the depth of the source and $v_{\text{fast}}$ is the averaged propagation speed of the fast wave in the high-$\beta$ region. For simplicity, here we have assumed the constancy of the propagation speed and neglected the effect of refraction and reflection. After arriving at the $\beta = 1$ layer, a portion of the fast wave is converted to the slow wave (Cally 2001) which then propagates along the field. For that reason, we can observe the radially propagating wave patterns when the slow mode reaches the detection layer. With the use of this effect, we can re-write the Equation (2.2) as follows:

$$v_z = -i\frac{k_z c_s^2}{\omega^2} A_m J_m(k_r r) \exp i \left(k_z z + m\theta - \omega\left(t - t_A(r)\right)\right). \tag{2.5}$$

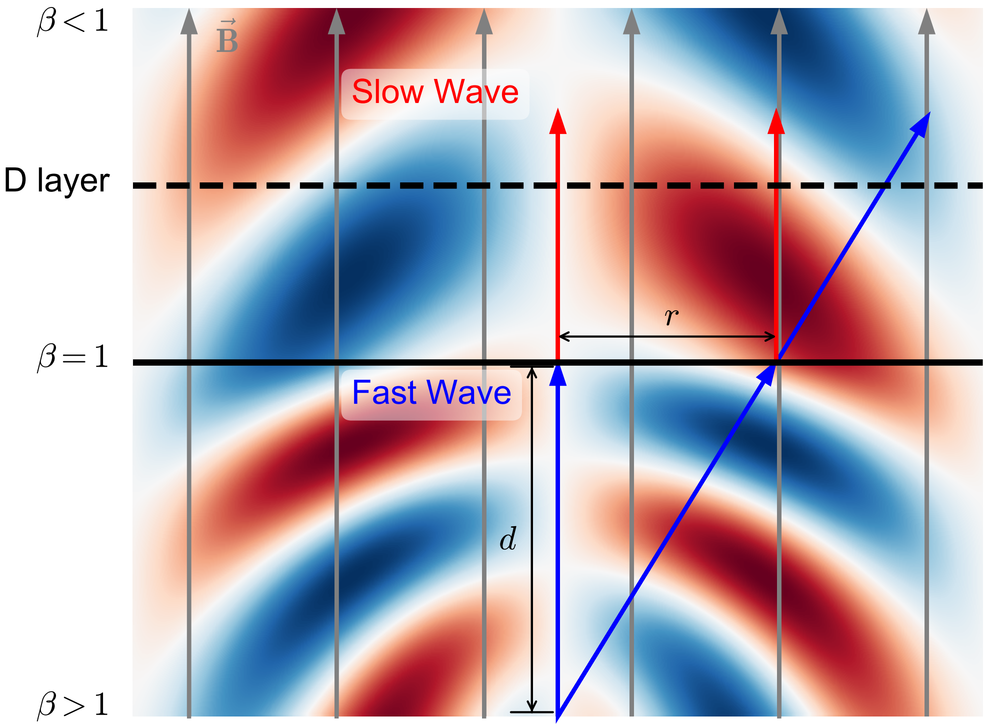

Figure 2.2 Schematic images of the longitudinal velocities $v_z$ in the $m = 1$ mode in the $x - z$ plane. The driving source of the wave is located at the center of the bottom. Blue (red) color represents the upflows (downflows). The black solid line indicates the $\beta = 1$ layer and the dashed line denotes the detection layer (D layer). Magnetic field lines are shown by the gray arrows. The propagating direction of the fast (slow) wave is shown by the blue (red) arrow.

As the wave frequency is constrained by the observation, we can derive the wave numbers $k$ for each azimuthal mode $m$ from the dispersion relation of (Edwin & Roberts 1983)

$$\rho k_{r,e}\left(\omega^2 - k_z^2 c_A^2\right)\frac{K_m'(k_{r,e}R)}{K_m(k_{r,e}R)} = \rho_e k_r\left(\omega^2 - k_z^2 c_{A,e}^2\right)\frac{J_m'(k_r R)}{J_m(k_r R)}, \tag{2.6}$$

where the subscript $e$ represents the exterior of the flux tube, $K_m$ is the modified Bessel function of the second kind, $K_m'$ is its derivative and $R$ is the radius of the tube, which is $5''$ in our case. We take $\omega = 2\pi/160\ \mathrm{s}^{-1}$ from the observation, $c_s = 9\ \mathrm{km\ s}^{-1}$ from Maltby et al. (1986), $c_A = 300\ \mathrm{km\ s}^{-1}$ from Khomenko & Collados (2006), $c_{s,e} = 1.5c_s$ and $c_{A,e} = 0.5c_s$ from Edwin & Roberts (1983), then the $k$ is approximately $4.36\times10^{-6}$ rad $\mathrm{m}^{-1}$ for all azimuthal modes.

Substituting these parameters into Equations (2.1) and (2.2), the ratio between the amplitudes of $v_z$ and $v_r$ is estimated as $v_z/v_r \sim 5\times10^3$ for all azimuthal modes. It means that every azimuthal slow-body mode is predominantly longitudinal in the chromosphere. Figure 2.3 shows snapshots of $v_z$ for $m = 0$, 1, and 2 modes in the $x - y$ plane with $d = 1600$ km and $v_{\mathrm{fast}} = 20\ \mathrm{km\ s}^{-1}$. For the case of $m = 0$, the ring-like pattern is generated, and this ring apparently propagates radially outward. On the other hand, $m = +1$ and $+2$ modes produce apparently rotating patterns in the counterclockwise direction with one- and two-armed structures, respectively. As the ring-like pattern of $m = 0$ mode propagates radially, the power of this changes with time and radius, while the power of non-zero modes depends only on the radius because the patterns of these modes do not move out.

To reproduce the observed one-armed spiraling pattern, we summed up perturbations with $m = 0$ and $m = 1$, which are the most powerful modes according to the Fourier analysis, with the amplitude ratio of $A_0/A_1 = 0.54$, the source depth of $d = 1600$ km and averaged propagation speed of $v_{\mathrm{fast}} = 20\ \mathrm{km\ s}^{-1}$. In addition, we introduce the reference time $t_0$ and reference angle $\theta_0$ terms to set the origin of the simulation, then the $t$ is replaced by $t - t_0$, and $\theta$ is substituted by $\theta - \theta_0$ in Equa-

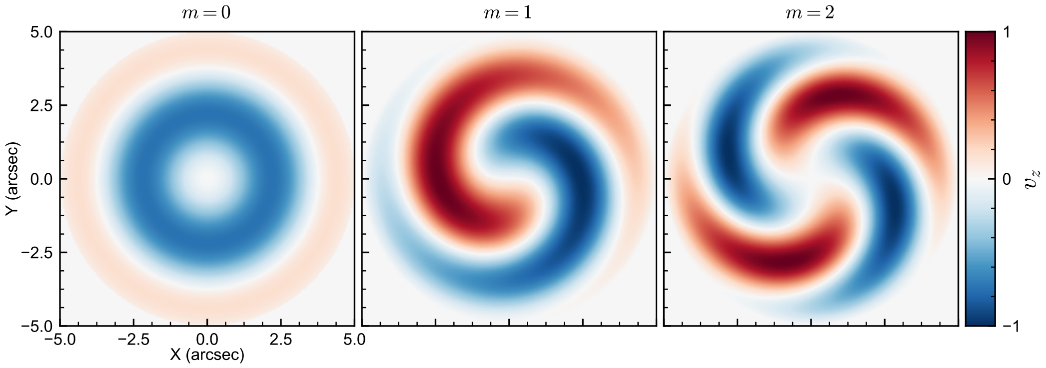

Figure 2.3 Snapshots of the simulated parallel velocity component for the azimuthal wave modes $m = 0$, $+1$ and $+2$ at $t = 0$ in $x - y$ plane. Speeds are normalized by the amplitude of each mode.

tion 2.5. Figure 2.4 indicates that the temporal evolution of the one-armed SWP from the observation (top) can be fairly well modeled by the simulation (bottom) with $t_0 = -20$ s and $\theta_0 = 170°$. Like the observation, the simulation can make the one-armed SWP. The red or blue arms abruptly change the trajectory to inward around $x = 2''$, $y = 1''$ in both the observation and the simulation.

We can successfully model the observed two-armed SWP as well. Because the wave power is concentrated at $m = 0$ and 2, we reproduce this pattern by summing up $v_z$ of $m = 0$ and $m = 2$ with the amplitude ratio of $A_0/A_2 = 0.54$, the reference time of $t_0 = 30$ s, and the reference angle of $\theta_0 = 30°$. In this simulation, the source is located at 1600 km below the $\beta = 1$ layer and the averaged phase velocity is about 20 km s$^{-1}$. Figure 2.5 represents the temporal evolution of the two-armed SWP. The observation and simulation show quite similar two-armed spiraling features. The two blue and red arms abruptly move inward around $x = -1''$, $y = 2.''5$ and $x = 1''$, $y = -2.''5$.

## 2.4 Discussion

In this chapter, for the first time, we have presented a model that can explain the observed SWPs as slow magnetohydrodynamic (MHD) waves in an untwisted magnetic field. In our model, the apparently rotating pattern is associated with the superposition of non-zero-$m$ azimuthal slow modes. A non-zero-$m$ mode has a right-handed (left-handed) helical shaped wavefront for the case of positive (negative) $m$. As this wave propagates upwardly along the straight field in a vertical magnetic flux tube, the wave pattern observed at some height shows an apparent rotation in the counterclockwise (clockwise) direction. This kind of a rotating wave pattern was observed for the case of $m = 1$ kink mode (Jess et al. 2017), and the related vortex dislocations were detected in a time-distance map along the slit placed in the center of the axis (López Ariste et al. 2016).

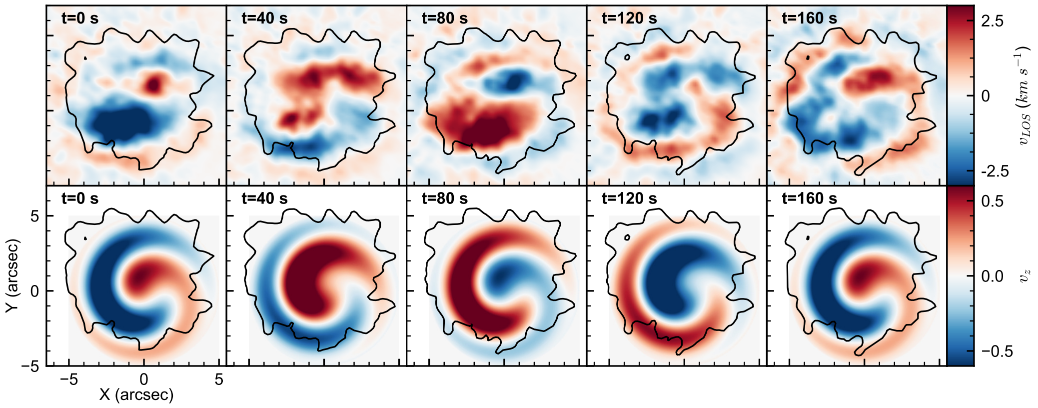

Figure 2.4 Temporal evolution of observed (top) and simulated (bottom) one-armed SWP from 17:17:20 UT to 17:20:00 UT. The observed Doppler maps are filtered in frequency bands from 5.5 to 9 mHz. The speeds in simulation are normalized by the maximum value. The boundary of the pore is shown by the solid line in both cases.

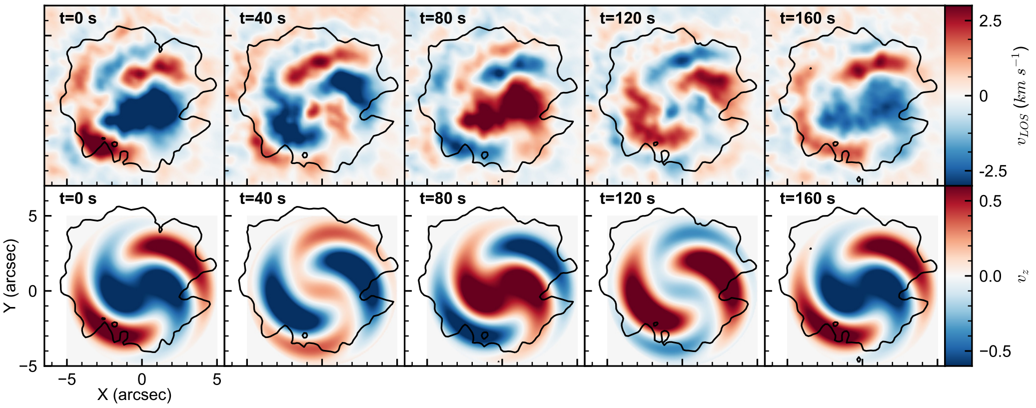

Figure 2.5 Similar to Figure 2.4, but for the case of two-armed SWP from 17:44:07 UT to 17:46:47 UT.

The spiral structures and outward propagating wave patterns are formed by the internal driving sources, i.e. situated inside the magnetic flux tube forming the umbra, which are placed below the photosphere. Beacause the wave propagates quasi-isotropically in the high-$\beta$ region, the longer the horizontal distance from the wave source to the observation point, the later the wave arrives. The difference in the arrival times in the photosphere results in an apparent radially moving ring pattern in the case of $m = 0$ (sausage) mode. In non-zero-$m$ modes, the trailing spiral arm structures are formed because of the wave patterns rotate earlier as it is closer to the axis of the waveguiding flux tube. The number of arms depends on the absolute value of $m$. Thus, the observed apparent rotating spiral arms are not caused by the wave propagation in the azimuthal direction, but by the oblique, spiral-shaped wavefront of vertically propagating perturbations.

Because of the abrupt spiraling motion of the one-armed spiral, Su et al. (2016) proposed that this pattern may be caused by the reflection at a light bridge. In our case, however, there was not light bridge at all and, nevertheless, such SWPs were detected. Our simulation clearly shows that the spiraling patterns are formed by the superposition of the wavefronts of an $m = 0$ and a higher-$m$ modes. The one-armed SWP is generated by an $m = 0$ sausage mode and an $m = 1$ kink mode, and the two-armed SWP is formed by an $m = 0$ sausage mode and an $m = 2$ fluting mode.

We surmise that the driving source of a SWP may be associated with the downflows caused by the local magnetoconvection inside the sunspot. According to the 3D radiative MHD simulation of Kitiashvili et al. (2019), acoustic waves can be generated by the converging downflows at 1.5 Mm beneath the surface inside a pore. This depth is very close to the depth of the source used for our model. Furthermore, as there is no time lag between the two azimuthal modes in our simulation, it seems that these modes are excited simultaneously by the same driver.

We need to stress that the kink wave in a sunspot umbra or a pore considered here should not be confused with the kink waves studied in coronal loops. In the loop, the kink mode is a transverse wave (Aschwanden et al. 1999; Nakariakov et al. 1999), while the sunspot kink mode considered here is a longitudinal wave associated with a slow magnetoacoustic wave (López Ariste et al. 2016; Jess et al. 2017). As a slow wave in a low-$\beta$ plasma, the kink wave in a sunspot is mainly characterized by parallel, field-aligned plasma flows. The radial flows, $v_r$, in this wave are quite small, because the $\omega^2 - k_z^2 c_s^2$ factor in Equation (2.1) tends to zero as the phase speed is about the sound speed. Another difference is connected with the wave polarization. Kink oscillations of coronal loops are usually linearly polarized, while the spiral wave structure in a sunspot requires the kink oscillation to be circularly polarized; i.e. the azimuthal wavenumber is $m = +1$ or $m = -1$. The sign is determined by the sense of rotation of the wavefront.

Because the mechanism does not require additional assumptions such as the flux tube twisting or rotation, we expect that such SWPs may be generally detected in any sunspots. As we accumulate the observation of those patterns, we can infer more physical parameters in sunspots such as propagating speed of fast wave and depth of the wave driving source. Furthermore, those wave patterns can be considered as the evidence of the internal excitation of 3 minute oscillations in sunspots. Further study of the SWPs may provide us with the clues to how magnetoconvection inside a sunspot generates such waves.

# Chapter 3

# Statistical Analysis of Spiral-Shaped Wave Patterns in Sunspot Umbrae[1]

## 3.1 Introduction

Intensity and velocity oscillations are one of the prominent magnetohydrodynamic (MHD) features observed in sunspot umbrae. After the first observation of chromospheric umbral oscillations was reported by Beckers & Tallant (1969), it was found that the predominant oscillation period is 2-3 minutes in the chromosphere (Beckers & Schultz 1972) and above (Gurman et al. 1982; O'Shea et al. 2002). Sunspot waves have been considered slow MHD waves that propagate upwards along the magnetic field with the group speed around sound speed (Centeno et al. 2006; Felipe et al. 2010) even to the corona (Maltby et al. 1999; O'Shea et al. 2002; Sharma et al.

---

[1] Most of the contents in this chapter were written as a separate paper: Juhyung Kang, Jongchul Chae, Jooyeon Geem, *"Statistical Analysis of Spiral-Shaped Wave Patterns in Sunspot Umbrae"*, 2023, Submmited to ApJ

2017). These waves have been thought to excited by the magnetoconvection such as umbral dots (Jess et al. 2012; Cho et al. 2019) and light bridges (Yurchyshyn et al. 2015; Chae et al. 2017).

Sometimes the umbral waves display outstanding spiral-shaped wave patterns (SWPs) on the image plane. Sych & Nakariakov (2014) first detected the SWPs with two arms at different atmospheric levels ranging from the temperature minimum to the corona. These SWPs were characterized by the rotating pattern and the radially propagating arms. Sych & Nakariakov (2014) concluded that these patterns are basically consistent with the umbral slow MHD waves propagating upwards. Subsequently, Su et al. (2016) reported one and multiple-armed spiral structures in the chromosphere. They suggested that the spiral structure may be related to the reflection of wavefronts and magnetic twists. However, Felipe et al. (2019) concluded that the twisted field is not the main cause even though it can affect the shape of the wavefronts. Jess et al. (2017) interpreted the observed rotating pattern as a two-dimensional pattern of slow body waves with non-zero azimuthal numbers. This pattern, however, cannot reproduce the spiral-arm structures.

Recently, Kang et al. (2019) suggested a model that the spiral-shaped pattern results from a non-axisymmetric disturbance in the interior. According to this model, the apparent radial outward motion and spiral-shaped arms are related to a source located in the deep interior. If a disturbance occurs at a deep subsurface region, i.e. high-$\beta$ region, in the sunspot, fast (acoustic) waves are excited, propagate quasi-isotropically initially, and then become refracted into the outward direction, eventually reaching the $\beta \sim 1$ layer (Zhao et al. 2015). The difference in the ray path among the wavefronts makes the phase vary as a function of radial distance. The resulting phase difference is responsible for radial motion and spiral arms. The existence of the non-zero azimuthal mode generates the rotating motion, and the direction of the rotation is determined by its sign. In addition, the absolute value of the mode is related to the number of arm structures. The inward motion near the center of the SWPs is produced by the superposition of the axisymmetric ($m = 0$) with the non-axisymmetric mode. According to this interpretation, the morphology of the SWPs is irrelevant to the magnetic twist. This conclusion was supported by comparing the patterns generated in a uniform magnetic field and the waves in a twisted magnetic field (Wu et al. 2021).

The success of this model implies that these SWPs may occur in any sunspot regardless of magnetic structures only if a disturbance excites non-axisymmetric waves. Note that, the previous observational results were obtained from a limited number of samples. We raise several questions to infer the general properties or to compare the umbral oscillations. How frequently do the SWPs occur? What are the observational differences between the SWPs and the umbral waves? Is there any hemispheric dependence on the rotation direction? Is the size of the umbra associated with the generation of these patterns? How deep is the source? With these questions in mind, we investigate the statistics of the observational parameters in this chapter.

In section 3.2, we describe the data and how to define the SWPs. In section 3.3, we show the results. In section 3.4, we summarize the results and present our discussion.

## 3.2 Data and Methods

In this chapter, we used 304 Å line EUV data taken by the Atmospheric Imaging Assembly of the Solar Dynamics Observatory (SDO/AIA; Lemen et al. 2012) from 2013 to 2018. The SWPs are observable at the different bandpass of AIA covering from the temperature minimum to the corona, but are best visible in 304 Å with the maximum power, which covers the upper chromosphere and the transition region (Sych & Nakariakov 2014).

Here, we examined 496 sunspots satisfying the following criteria. First, they have to be located near the disk center with longitudes of $|\phi| \leq 30°$, i.e. $\mu \leq 0.87$, on the intensity images obtained with the Helioseismic and Magnetic Imager (HMI; Schou et al. 2012) as a supplementary data. Second, they should have umbrae larger than 4.5 Mm for spiral arms to be spatially resolved. Third, they should have a simple shape, either a circle or an ellipse, not having light bridges and jet events that can modify or shade wave patterns. Finally, they have to be observed for at least two hours, not being disturbed by any impulsive events such as flares.

We automatically identified SWPs in the sunspot umbrae using a four-step algorithm in the following. First, we extract the intensity oscillation in the frequency band of 5-9 mHz by applying the Fourier bandpass filter (Figure 3.1b). This frequency band highlights chromospheric umbral oscillations because most of the wave power is concentrated near cutoff frequency (Chae et al. 2019).

Second, we determine the center of the patterns by locating the local peak of $C(x, y) = \boldsymbol{\nabla} \cdot \boldsymbol{v}/|v|$ that is stable enough, changing less than one arcsecond over one minute (panel c). Here $\boldsymbol{v}$ is the velocity vector determined with the differential affine velocity estimator (DAVE) code (Schuck 2006). If the spherical waves (fast waves) are driven below the surface, as mentioned in section 3.1, the phase difference of wavefront arriving at the equipartition layer ($\beta \sim 1$) makes a pattern diverge out of a point. This point is identified by a local peak of $C(x, y)$.

Third, we obtain the spatially-filtered intensity by extracting only the intensity oscillation of the azimuthal mode of maximum power (panel e). The azimuthal mode of maximum power is determined from the azimuthal Fourier transform (panel d) applied to the one-dimensional temporally filtered data taken along the blue dashed circle. Since the number of spiral arms reflects the spatial distribution of the pattern (Kang et al. 2019), this number, in fact, becomes equal to the derived azimuthal mode of the maximum power.

Finally, we obtain the temporal information of SWPs from the wavelet power

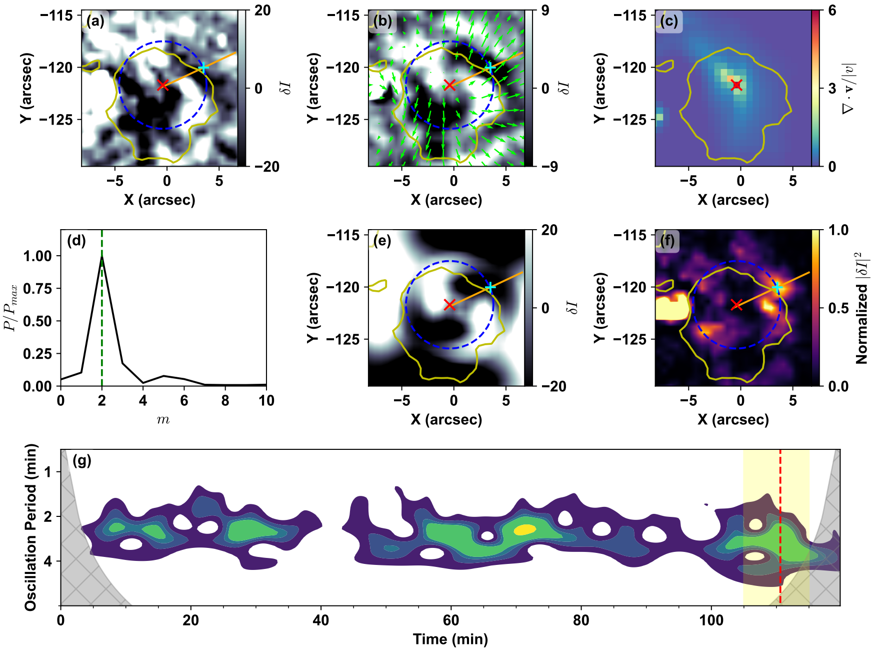

Figure 3.1 Detection method to identify the SWPs. (a) Intensity fluctuation image in NOAA 11658 obtained on 2013 January 18 at 15:49:19 UT with the SDO/AIA 304 Å band. (b) Temporally-filtered image in a frequency band of 5-9 mHz of the sunspot. (c) $\boldsymbol{\nabla} \cdot \boldsymbol{v}/|v|$ map of the filtered image. (d) Azimuthal power spectrum calculated along the blue dashed circle. (e) Spatially filtered $m = 2$ mode intensity fluctuation map. (f) Normalized temporally averaged filtered intensity power map (g) Wavelet power spectrum of m=2 mode intensity map at the cyan '+' position. The yellow contour in panels represents the umbra-penumbra boundary. The green arrows in panel (b) display velocity vectors $\boldsymbol{v}$. The red 'X' symbol represents the center of the SWPs, and the cyan '+' symbol marks the position where the intensity power is maximized. The orange line shows the slit of the time-distance map, and the blue dashed circle illustrates the circular slit of the time-angle map shown in Figure 3.2. The angle of the orange line from the x-axis is equivalent to the gradient between the center (x) and the maximum intensity (+), and the radius of the blue dashed circle is the same as the distance. The green dashed line in panels (d) marks the azimuthal mode of maximum power. The red dashed line in panel (g) shows the equivalent time of the image shown in other panels. The yellow region in panel (g) represents the lifetime of the detected SWP.

spectrum of the spatially filtered intensity at the position of maximum intensity power (panel g). In the intensity power map (panel f), we mark the position of the maximum intensity power by the cyan '+' symbol. At this position, we calculate the wavelet power spectrum of the spatially-filtered intensity and identify the wave packets. For 2 hours duration, we often identify more than one SWP in the same sunspot. Note that all the steps above are automatically done. As this automatic detection may not be perfect, we examine every detection by eye and exclude the detected patterns that are too complex for the spiral arms to be clearly displayed.

We derive the intensity oscillation period and the lifetime of an SWP from the wavelet power spectrum. The oscillation period comes from the peak frequency of the wave packet, which is usually different from the morphological period of the SWP that is equal to the azimuthal mode times the oscillation period. We set the lifetime of the SWP to twice the full width at half maximum (FWHM) time of the wave packet that may be close to the duration when the oscillation has power significantly above the noise. This oscillation period and lifetime may depend on the distance of the measurement point from the center because high-frequency waves are more confined at the center of the axis (Sych & Nakariakov 2014), and these high-frequency waves can propagate faster than low-frequency that linger for a long time (Kalkofen et al. 1994; Chae & Goode 2015). We put the measurement point on the position of maximum intensity power of the azimuthal mode, as we are interested in the SWP.

We calculate the apparent speed of the pattern from the time-distance map of intensity fluctuation and the time-angle diagram (Figure 3.2). We produce the time-distance map by stacking all time data taken from the slit that is directed from the oscillation center (red ×) into the point of the maximum power of $|\delta I|^2$ (cyan +). From the gradient of ridges visible in the time-distance map, we derive the speed of apparent radial motion. Similarly, a time-angle diagram was produced by stacking

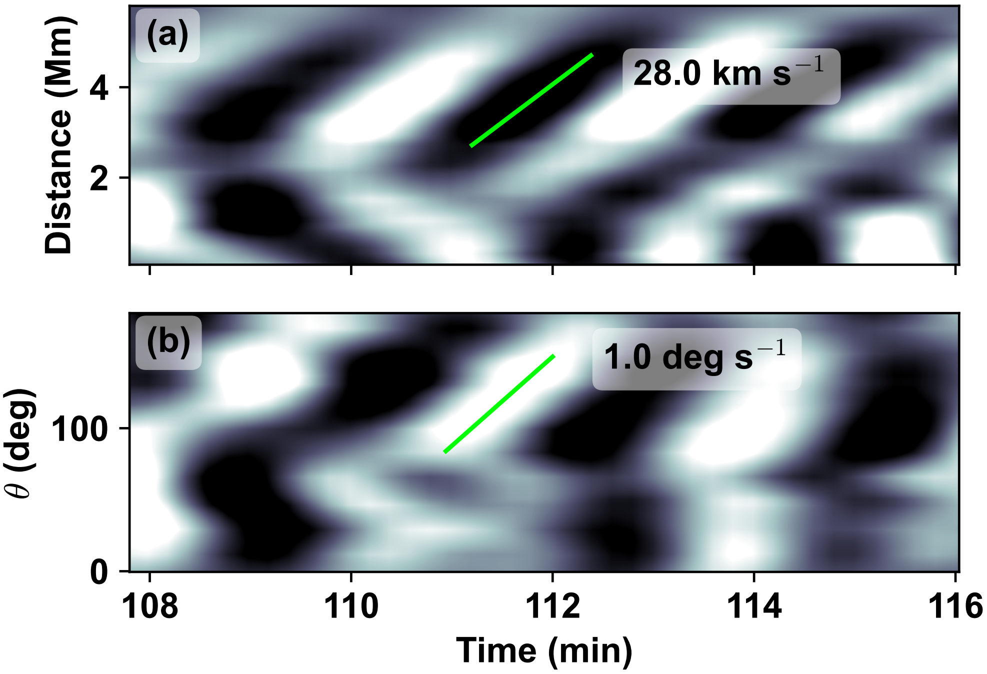

Figure 3.2 Time-distance map (a) and time-angle diagram (b) derived from the orange slit and the blue dashed circle in Figure 3.1b, respectively. The color scale is the same as the Figure 3.1b. The green solid line represents the gradient of the ridge.

all time data taken along the blue dashed circle. The radius of the circle is the same with the length between two positions. The apparent angular speed ($d\theta/dt$) was measured from the gradient of the ridges seen in this map, and the rotation direction comes from its sign. We convert the angular speed to the rotation period using the relationship $P_r = 360^\circ/(d\theta/dt)$.

## 3.3 Results

We found a total of 241 SWPs in 140 sunspots. Among them, 192 SWPs had one spiral arm and 48 SWPs had two arms. Only one SWP had three arms, which was not included in our statistical analysis because of its rarity. The detection rate of SWPs is 0.24 per hour. In other words, if a sunspot is observed for 4 hours, at least one SWP can be detected. This is significantly lower than the occurrence of the consecutively generated umbral oscillations.

Figure 3.3 illustrates the time variation of two SWPs rotating in opposite directions with different spiral arms that occurred at the same sunspot umbra in NOAA 11658 on 2013 June 18. Upper panels display the spiral patterns with one arm and lower panels exhibit two-armed cases. Two cases clearly showed the apparent radial moving spiral arms far from the center of the SWPs. The two SWPs swirled in opposite directions: the one-armed SWPs rotated in a clockwise (CW) direction and the two-armed cases rotated in a counterclockwise (CCW) direction. These features are very similar to the SWPs previously reported based on the Doppler velocity (Felipe et al. 2019; Kang et al. 2019).

We find that the rotation direction of the SWPs does not depend on the hemisphere and the latitude as indicated by the histograms of sunspot latitude for the two rotation directions shown in Figure 3.4a. In order to statistically confirm that the rotation direction of the SWPs is independent of the hemisphere and the latitude, we examine the hypothesis that the two different rotation samples are drawn

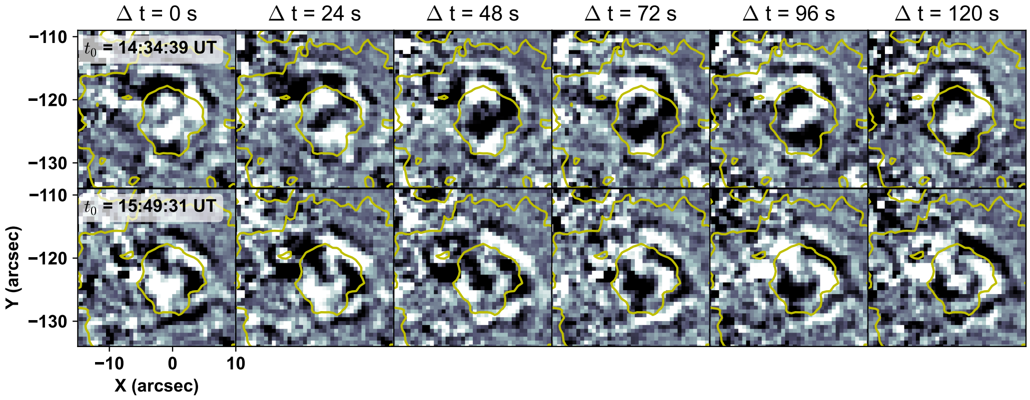

Figure 3.3 Temporal evolution of one-armed SWPs (upper row) and two-armed SWPs (lower row) occurred in the same sunspot shown in Figure 3.1 but at different times $t_0$. The images are filtered in a frequency range of 5-9 mHz. The yellow inner contour indicates the umbra-penumbra boundary and the outer contour represents the boundary of the penumbra.

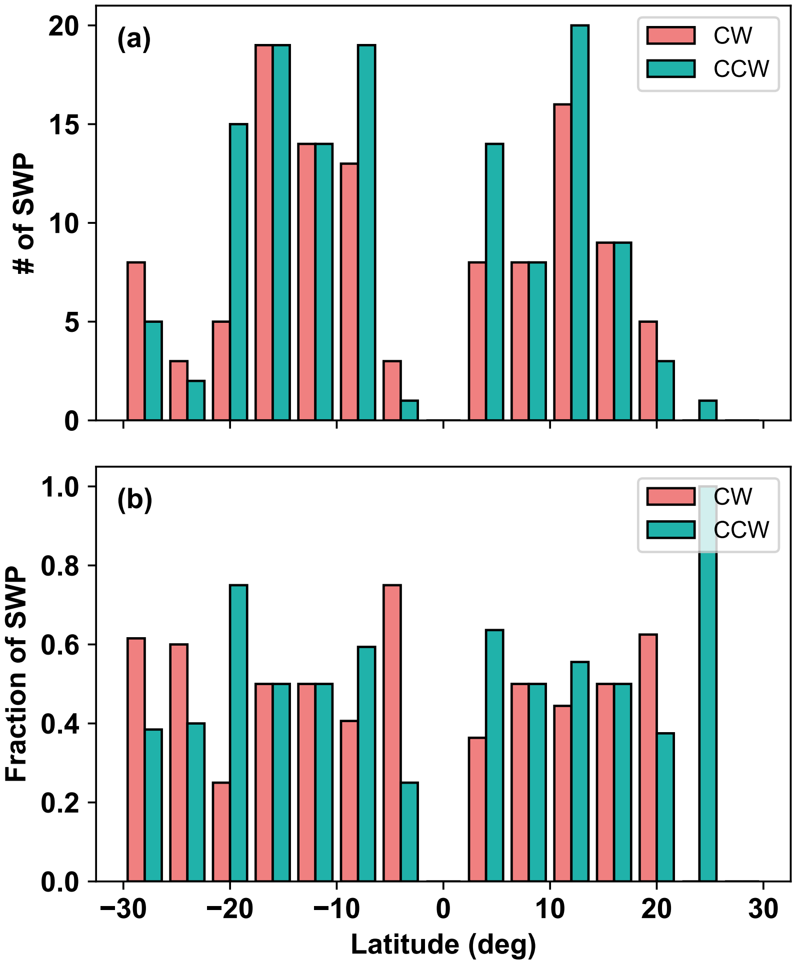

Figure 3.4 Histograms of sunspot latitudes for SWPs rotating in clockwise (red) and counterclockwise (green) directions. The top histogram shows the number distribution of two rotation direction samples, and the bottom histogram shows the fraction of them. The bin size is 4 degree.

from the same populations by applying the two-sample Anderson-Darling (AD) test to two rotation samples (see Anderson & Darling 1952). As a result, we find that the probability value (p-value) of the AD test is higher than 0.25, which means that we have no reason to reject the hypothesis. Moreover, we find that CW SWPs and CCW SWPs are almost equal in number at every latitude in the range of 10 (or$-10$) to 20 (or $-20$) degree where the number of sunspots is large enough (Figure 3.4b).

Does the occurrence probability of a SWP depend on the size of the sunspot umbra that hosts it? Figure 3.5a indicates that the umbral sizes are mostly (90 %) distributed between 3.0 and 15.5 Mm with a mean of 9.9 Mm and a standard deviation of 4.4 Mm. Within the range of 3.0 to 15.5 Mm, we find the tendency that the larger the sunspot umbra is, the higher the occurrence probability of a one-armed SWP is (panel b). We confirm that this tendency is statistically meaningful. If this tendency would be nothing but a result of statistical flucutation from a uniform distribution, the p-value of the AD uniformity test should be higher than at least 0.05. However, our calculation yields a smaller value of 0.038, so the one-armed SWP relates to the umbral size. Similarly, we find that the occurrence probability of a two-armed SWP is independent of the umbral size with the p-value of 0.24 obtained from the AD uniformity test. This tendency may be related to the number of the source of the wave because it can increase with the sunspot size according to the internal excitation model.

Figure 3.6 presents the number distribution of the parameters determined in the SWPs of the two types, respectively. First, we find that oscillation periods of the SWPs of the two types are about the same: the period of one-armed SWPs is $148 \pm 35$ seconds, and that of two-armed SWPs is $151 \pm 37$ seconds (panel a). This oscillation period is comparable to the period of chromospheric 3-minute umbral oscillations (see the reviews of Khomenko & Collados 2015), which is not surprising at all because the SWPs are regarded as a specific pattern of slow magnetoacoustic

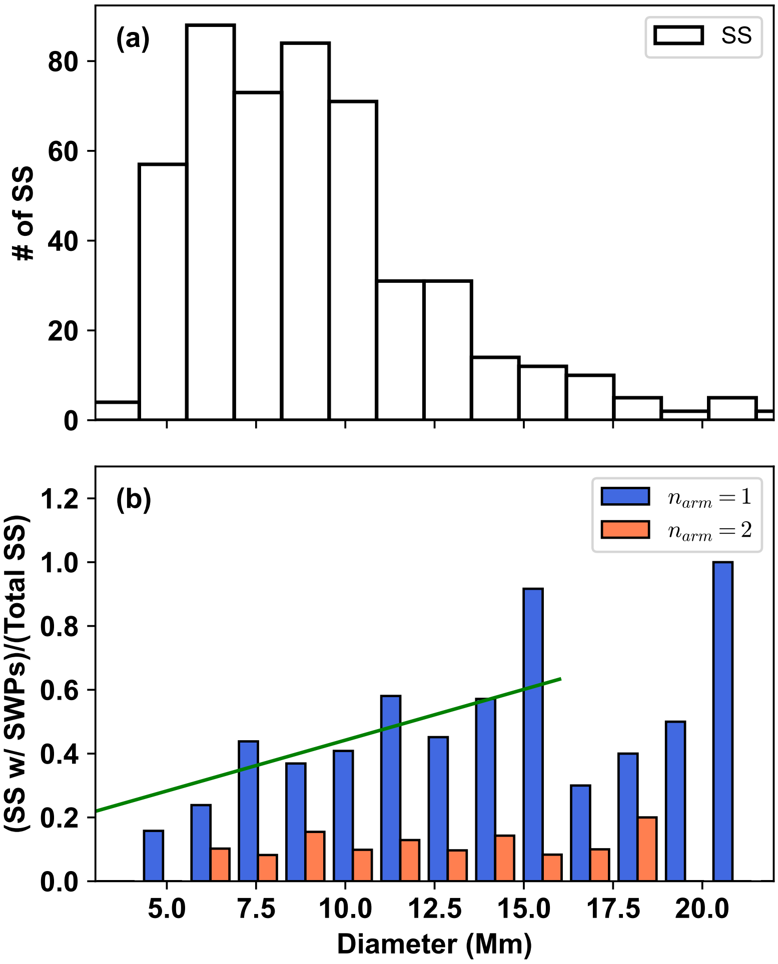

Figure 3.5 Histogram of the umbral size of the examined sunspots (SSs) (a) and the distribution of the umbral size of the sunspots with one-armed SWPs (blue) and two-armed SWPs (orange) against the total examined sunspots (b). The histogram only shows the data with a size in the range of 2.5-22.5 Mm, and the bin size is 1 Mm. The green line represents the increasing trend of the one-armed SWPs with a gradient of 0.032 and a y-intercept of 0.124.

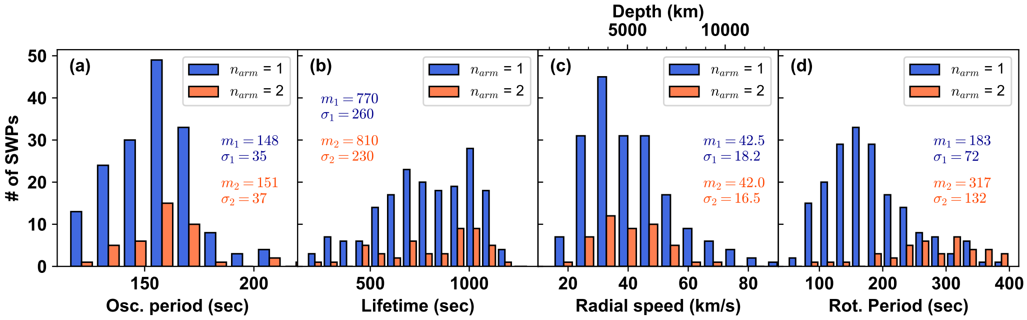

Figure 3.6 Histograms of the oscillation period (a), lifetime (b), radial speed (c), and rotation period (d). The blue represents the one-armed spiral patterns and the orange represents the two-armed cases. The mean value (m) and standard deviation ($\sigma$) are shown in panels, where subscripts 1 and 2 represent the one-armed SWP and two-armed SWP. The bin size of (a) is 11.25 seconds, (b) is 75 seconds, (c) is 6.75 km $s^{-1}$, (d) is 23.3 seconds.

waves propagating along magnetic fields (Sych & Nakariakov 2014; Felipe et al. 2019). As a matter of fact, the SWP at each location can be identified as one-dimensional umbral oscillations that have their phase depending on their location inside the sunspot.

Next, we find from Figure 3.6b that the SWPs of the two types have almost the same lifetime: the lifetime of one-armed SWPs is 770 ± 260 seconds, and that of two-armed SWPs is 810 ± 230 seconds. These are roughly five times the oscillation period, being comparable to the lifetime of the one wave packet of umbral oscillations of around 10-20 minutes (e.g. O'Shea et al. 2002; Chae et al. 2019), and the duration of the vortex waves of about 15 minutes (López Ariste et al. 2016).

Figure 3.6c shows the histograms of apparent radial speed for one-armed SWPs and two-armed SWPs, respectively. The measured speed is $42.5 \pm 18.2$ km $s^{-1}$ for the one-armed SWPs and $42.0 \pm 16.5$ km $s^{-1}$ for the two-armed pattern, indicating that there is no practical difference in the speed between them. As the apparent radial speed may depend on the depth of the source according to the internal excitation model (Felipe & Khomenko 2017; Cho & Chae 2020), the source depth can be inferred from the pattern speed. Using the eikonal method following the equations (3) to (7) in Cho & Chae (2020), we have calculated the ray path of waves driven beneath the surface. As a result, we have obtained the theoretical relationship between the depth of the source and the radial speed, as shown in Figure 3.7. Using this relation, we find that the two-sigma range of speed from 10 km $s^{-1}$ to 75 km $s^{-1}$ corresponds to the range of depth from 2 to 10 Mm, with the mean depth being about 6 Mm, irrespective of the type.

Finally, the rotation period of the one-armed SWPs is $183 \pm 72$ seconds which is half of the two-armed SWPs of $317 \pm 132$ seconds and is comparable to the result of the $m = 1$ slow magnetoacoustic mode previously obtained by Jess et al. (2017) (Figure 3.6d). The observed dependence of the rotation period on the azimuthal

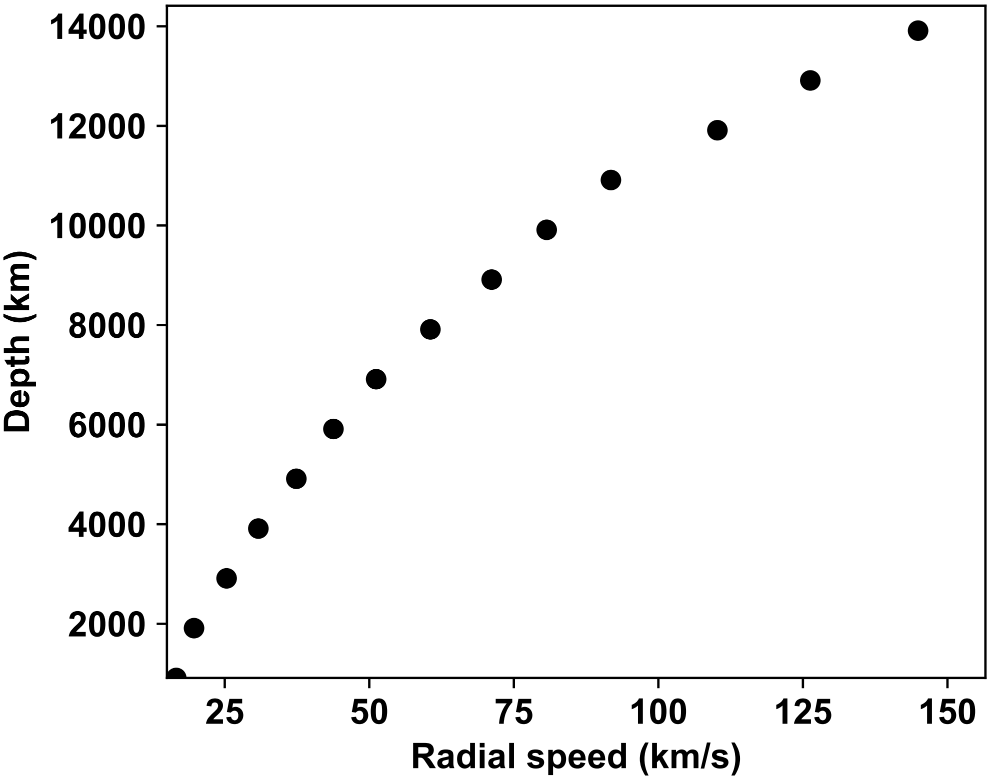

Figure 3.7 Apparent radial speeds for different depths of wave sources.

mode is very compatible with the theoretical expression,

$$P_r = \frac{360^\circ}{d\theta/dt} = \frac{m}{\omega}, \tag{3.1}$$

where $\omega$ is the oscillation frequency that equals the inverse of the oscillation period $(2\pi/P)$. This relation can be easily derived from the constancy of the phase $kz + m\theta - \omega t$ in the wave equation of Kang et al. (2019) with $z$ being constant. Here $\omega$ is independent of the azimuthal mode $m$ (see Figure 3.6).

We found relations between measured parameters from the scatter plots shown in Figure 3.8. When calculating each correlation value, we excluded the samples with any parameter outside three times standard deviations as outliers, that is, with oscillation period longer than 300 seconds, radial speed faster than 95 km $s^{-1}$, umbral size larger than 25 Mm and rotation period longer than 500 seconds. For the case of two-armed SWPs, the rotation period and the intensity oscillation period have a weak positive correlation (0.31) as described in equation (3.1), but the correlation is somewhat weak because of the measurement error. There are no significant correlations between other parameters. The oscillation period and the radial speed do not correlate because the two parameters come from different layers: the oscillation period depends on the cutoff frequency at temperature minimum, and the apparent radial speed may be determined from the source depth according to the internal excitation model. The radial speed is independent of the umbral size because the internal excitation source may be irrelevant to the size of the flux tube. If the converging plasma of the magneto-convection generates waves, the radial speed is relevant to the rotation period conserving the angular momentum but isn't. From these relations, we conjecture that the SWPs may be generated by random events, such as the turbulent motion in the high-$\beta$ region.

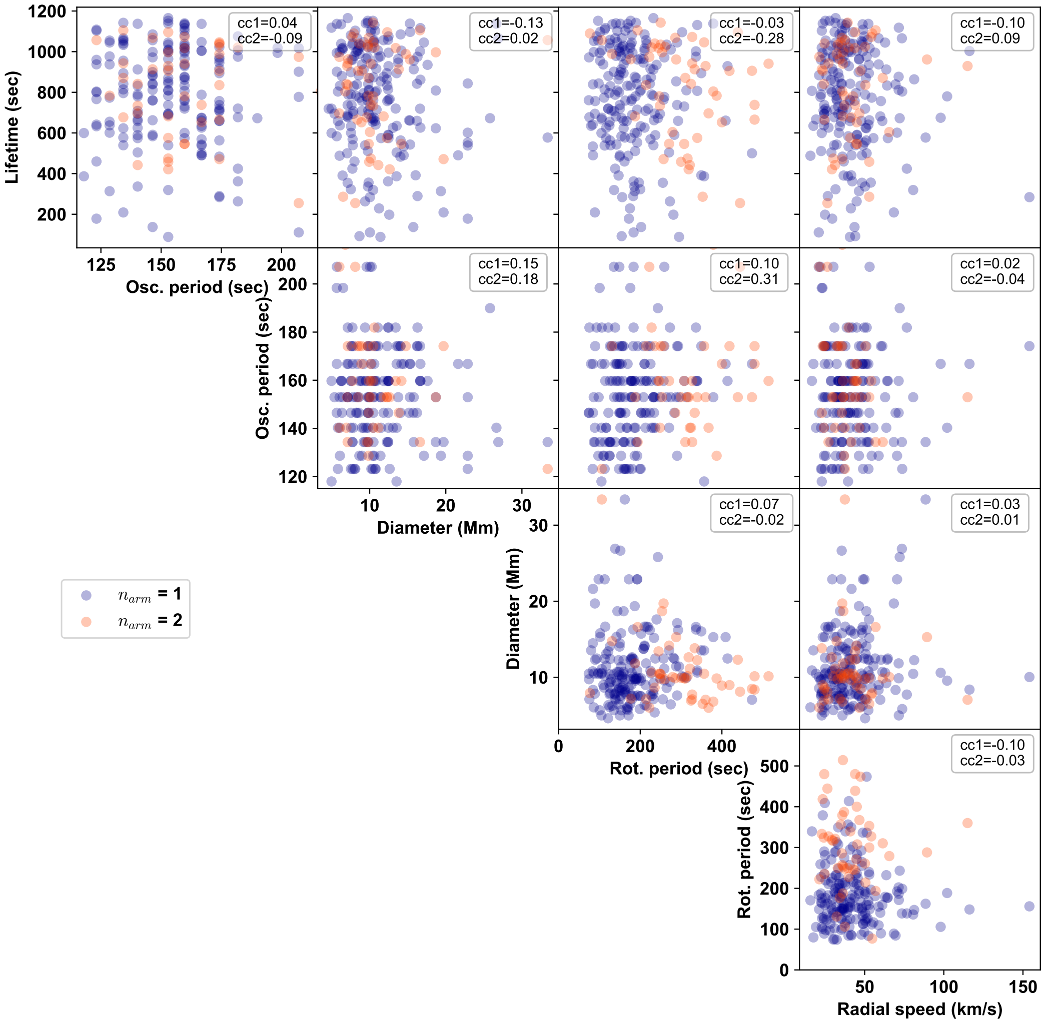

Figure 3.8 Scatter plots between measured parameters for one-armed SWPs (blue) and two-armed SWPs (orange). Pearson correlation values for one-armed SWPs (cc1) and the two-armed SWPs (cc2) are indicated in the upper right box on each panel.

## 3.4 Discussion

We investigated the observational properties of the spiral-shaped wave patterns (SWPs) by investigating 496 sunspots observed in the SDO/AIA 304 Å line. We developed a method to identify the spiral structures in a 2D image plane. The rotation direction of the patterns does not depend on hemisphere and latitude. The rotation period is proportional to the number of spiral arms. The SWPs persisted for about 780 seconds with the intensity oscillation period of about 150 seconds. The speed of apparent radial motion ranges from 10 to 75 km $s^{-1}$, which suggests a depth of 2 to 10 Mm, according to the model of impulsive excitation below the surface.

The most notable discrepancy between observation and our expectation is the low value of the detection rate. This discrepancy may come either from observational bias or physical reasons. Observationally, the SWPs occurring near the umbra-penumbra boundary are difficult to be identified. Since the waves over the umbra-penumbra boundary propagate along the inclined magnetic field lines as running penumbral waves, the observed wavefronts look different from the typical SWPs shown inside the umbral region. In addition, if several waves occur at the same time but at different positions, the observed waves can show complex patterns because of the interference. From the physical viewpoint, we note only the waves where $m$ mode dominates over $-m$ mode (where $m$ is a non-zero integer) are responsible for the rotating spiral arm structures. The waves with the balanced $+m$ and $-m$ modes cannot contribute to the rotating pattern because the rotating component is canceled out. Considering this, we expect that non-axisymmetric wave modes ($m \neq 0$) may exist much more frequently than SWPs in the umbrae.

It seems that the rotating pattern is relevant neither to magnetic twist nor to the Coriolis force. We observed the reversal of rotation direction in a sunspot in an hour, which can not be attributed to the reversal of magnetic twist in such a short time in the low-$\beta$ region. Therefore, it is very likely that the rotating direction is irrelevant to the magnetic twist. Meanwhile, if the Coriolis force is to be responsible for the rotating direction, there should be hemispheric dependence, which we could not find in our data. Thus it is likely that the source may be related to local turbulent motions if the SWPs are generated by the internal source.

It is possible to explain the measured radial speed if the SWPs originate from localized sources located 2 to 10 Mm below the surface. From the fast-moving pattern speed, Zhao et al. (2015) reported that the waves occurred at about 5 Mm beneath the surface. Analyzing the speed of the ring-like moving pattern with the eikonal method, Cho & Chae (2020) suggested that the depth of the wave driver is located between 1 and 2 Mm below. Using the same method, we estimated that the 20 km $s^{-1}$ radial speed of the SWPs observed in Su et al. (2016) corresponds to a depth of about 2.1 Mm, which is quite similar to the value of 1.6 Mm proposed in Kang et al. (2019). Rigorous numerical 2.5D MHD simulations suggested that the observed pattern speeds are in agreement with the waves that occurred between 1 and 5 Mm beneath the photosphere (Felipe & Khomenko 2017). Analyzing the acoustic events in the 3D radiative MHD simulations, Kitiashvili et al. (2019) have reported that the wave sources are located from 1 to 2.5 Mm below the photosphere inside the self-organized pore-like magnetic structure. Most recent observational studies have concluded that the mixed shallow ($\sim$ 2000km) and deep ($\geq$ 5000 km) sources excite the fast-moving pattern in one sunspot (Cho et al. 2021).

Based on our results, we suggest that the SWPs may be excited by random events below the surface. In addition, there may be non-zero azimuthal modes as well that may not rotate, unlike SWPs. Further systematic studies are required to investigate non-axisymmetric patterns of oscillations including SWPs.

# Chapter 4

# Chromospheric Umbral Oscillations Driven by the Resonance of Fast Magnetohydrodynamic Waves in the Subphotosphere

## 4.1 Introduction

Umbral oscillations are the most conspicuous magnetohydrodynamic phenomena in sunspot umbrae. After the first detection of intensity fluctuations in chromospheric umbrae was reported (Beckers & Tallant 1969), subsequent works have revealed that these oscillations are the slow waves propagating upwards from the photosphere to the corona with the group speed of around sound speed (Lites 1984; Centeno et al. 2006; Felipe et al. 2010; Khomenko & Collados 2015). The temperature-minimum at the bottom of the chromosphere in the gravitationally stratified medium acts as a high-pass filter of acoustic waves, and the wave power peaks around the cutoff frequency of about 6 mHz in the chromosphere (Centeno et al. 2006; Kalkofen et al. 1994; Chae & Goode 2015). A portion of low-frequency waves can propagate upwards by the effect of the temperature gradient (Chae & Litvinenko 2018), and the non-adiabatic heating and cooling such as radiation (Centeno et al. 2006; Chae et al. 2023).

Interestingly, even though the slow waves cannot propagate across the magnetic field, recent observational studies have reported that the waves appear to move across the magnetic field forming ring-like patterns (Zhao et al. 2015; Cho & Chae 2020; Cho et al. 2021) or spiral-shaped wave patterns (SWPs) (Sych & Nakariakov 2014; Su et al. 2016; Felipe et al. 2019; Kang et al. 2019). To interpret these features, the internal excitation model focused on a localized disturbance in the high plasma $\beta$ region beneath the sunspot surface (Zhao et al. 2015; Cho & Chae 2020). If the disturbance excites fast waves in the high-$\beta$ region, the waves propagate quasi-isotropically. The wavefront reaching the $\beta \sim 1$ region has a time delay as a function of horizontal distance, and this time delay makes ring-like patterns appear to propagate across the magnetic field (Zhao et al. 2015). After reaching the $\beta \sim 1$ region, a portion of the fast waves can be converted to the slow waves by the mode conversion process (Zhugzhda & Dzhalilov 1984; Cally 2001; Schunker & Cally 2006; Cally 2007; Cho & Chae 2020). Using this idea, the SWPs were also regarded as the waves excited by the point-like source generating non-axisymmetric modes beneath the photosphere (Kang et al. 2019).

Another model to explain the wave patterns is the resonance of the slow body waves (Stangalini et al. 2022). If the waves are trapped in the flux tube, the orthogonal eigenmodes of the resonance appear in the horizontal planes (Edwin & Roberts 1982, 1983; Roberts 2019). According to this model, the observed complex wave patterns in a large-scale sunspot were reproduced by the superposition of several simultaneous resonant modes of slow body waves (Stangalini et al. 2022). In the same way, the chromospheric oscillation patterns observed in circular and elliptical sunspots were identified (Albidah et al. 2022). Even though the slow wave resonance model can explain the patterns themselves, this model cannot explain why only a few resonant modes were detected in pore-like small-scale flux tubes (Morton et al. 2011; Jess et al. 2017; Keys et al. 2018; Kang et al. 2019) because an infinite number of modes of slow waves can be trapped in the flux tube (Edwin & Roberts 1982, 1983).

In this chapter, we propose the subphotospheric fast body wave resonance model that can reproduce the observed complex wave patterns in the chromosphere. Our model can also explain why less than four radial modes exist in small-scale flux tubes and why lots of radial modes can be detected in large-scale sunspots from the existence of the cutoff wavenumber.

## 4.2 Data and method

We analyzed a pore in NOAA 12078 located at (-301$''$, 162$''$) on June 3rd, 2014 from 16:49 UT to 17:56 UT taken with the Fast Imaging Solar Spectrograph (FISS (Chae et al. 2013b)) at the Goode Solar Telescope (GST), which is the same data analyzed previously in several studies (Chae et al. 2015; Kang et al. 2019; Chae et al. 2022). The observed pore is an ideal simple circular flux tube with a size of 7 Mm in diameter and a vertical magnetic field (Figure 4.1a). The time cadence of the data is 20 seconds with a spatial resolution of 0.16$''$ and a spectral resolution of 19 mÅ in a spectral domain -5 Å to 5 Å of H$\alpha$. The raw data is calibrated following the reduction pipeline described in detail by Chae et al. (2013b). Among the two wavebands of H$\alpha$ and Ca II 8542 Å, we only used the H$\alpha$ data in this chapter.

Figure 4.1a shows the continuum intensity map and the chromospheric intensity

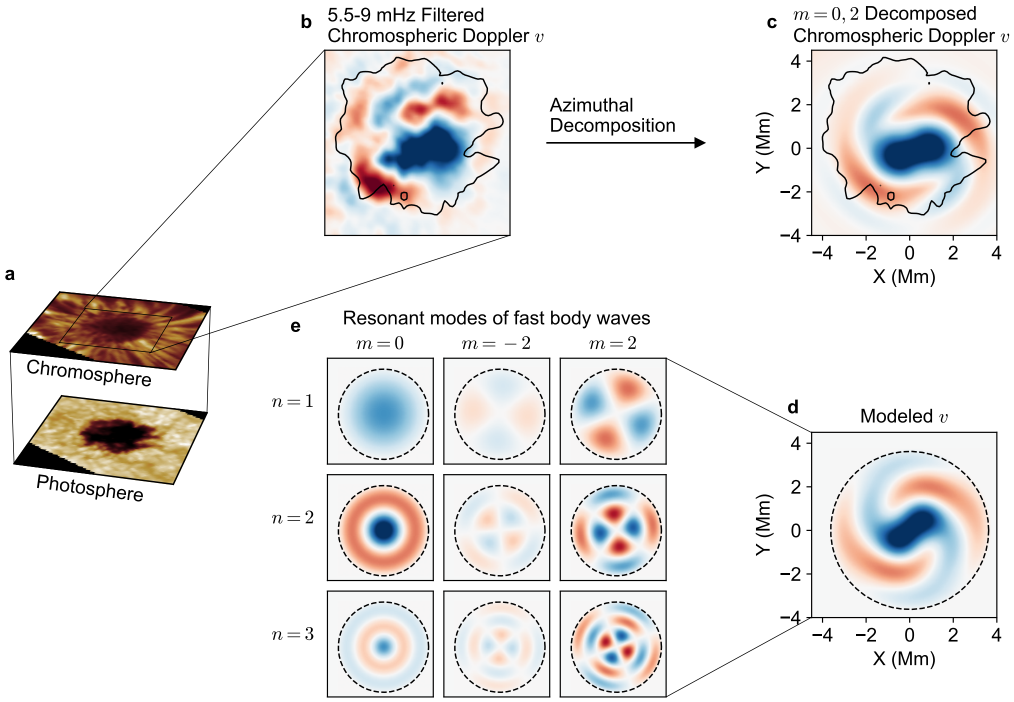

Figure 4.1 **Detection of non-axisymmetric oscillation patterns in a pore. a** The continuum intensity map of the GST/FISS constructed at the -3.5 Å of the H$\alpha$ line center and the chromospheric intensity map constructed at the line center at 17:44:07 UT on June 3rd, 2014. **b** Spiral-shaped wave patterns of the chromospheric Doppler velocity map temporally filtered in $5.5-9$ mHz. **c** Azimuthally decomposed spiral-shaped wave patterns for $m = 0$ and $\pm 2$ modes. **d** Modeled LOS velocity fluctuation map constructed by the superposition of three azimuthal modes and three radial modes for each azimuthal mode. **e** All resonant modes of fast body waves for the modeled LOS velocity map. The black contours shown in the panels **b** and **c** represent the boundary of the pore. The dashed circles in the panels **d** and **e** represent the flux tube boundary of the model. The red color in the panels **b-e** represents the redshift that is away from the observer, and the blue color represents the blueshift that is moving towards the observer. The color limit of the panels **b-d** is -3.5 to 3.5 km s$^{-1}$, and that for the panel **e** is -1.75 to 1.75 km s$^{-1}$. The temporal evolution of these patterns is shown in Figure 4.5.

map at the line center of the H$\alpha$. The line-of-sight (LOS) Doppler velocity of the H$\alpha$ line spectrum is measured from the lambdameter method (Chae et al. 2014). Here we only focus on the two-armed SWPs occurred at around 17:43:27 UT (Figure 4.1b).

The observed data is filtered temporally to increase the signal-to-noise ratio. The wavelet power spectrum of the line-of-sight (LOS) Doppler velocity at the center of the SWPs shows that most of the wave power is concentrated on the 2-3 minute band (Figure 4.2). The peak period is around 160 seconds, and a small portion of energy peaks in 1-minute and 5-minute bands. We apply a bandpass filter in the range of $5.5 - 9$ mHz that is equivalent to the 2-3 minute band by using a fast Fourier transform (FFT) to focus on the primary peak frequency of the LOS Doppler velocity map (Figure 4.1b and the top row in Figure 4.5).

Furthermore, we spatially filter the data to decompose each azimuthal mode $m$. The wave power of the two-armed SWP is concentrated at the azimuthal mode $m = 0$ and 2 (see Figure 1d in Kang et al. (2019)), but $m = 1$ mode can be negligible. We first transform the data coordinate to the polar coordinate at the center of the oscillation patterns using the interpolation and transformation matrix. Second, We perform the fast Fourier transform along the azimuthal direction for each point to filter the $m = 0$ and $m = 2$ modes. After filtering the azimuthal component, we return to data coordinates by applying the inverse coordinate transform from polar to cartesian coordinate. Figure 4.1c and the middle row in Figure 4.5 show the results.

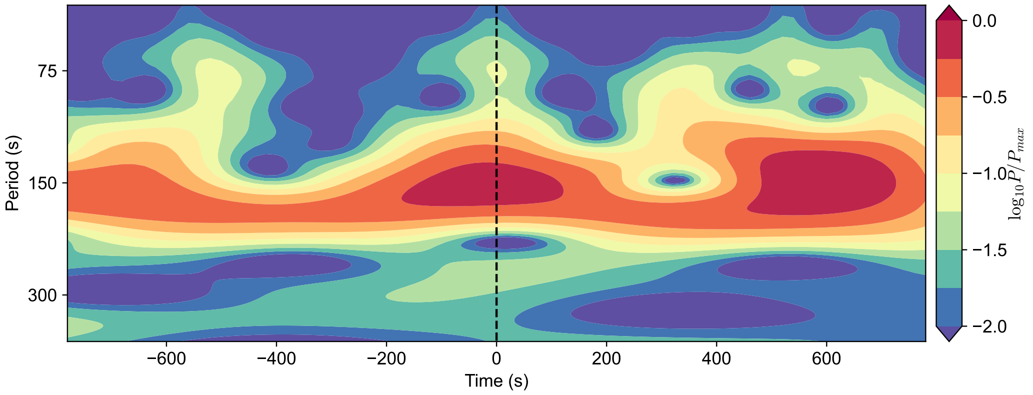

Figure 4.2 **Wavelet power spectrum.** Wavelet power spectrum of the Doppler velocity averaged over $3 \times 3$ pixels at the center of the oscillation patterns. The black dashed line represents the time t=0 at 17:43:27 UT which is the middle time of the wave packet of spiral-shaped wave patterns. Among the total observing duration (-3200 s to 780 s), the diagram shows only the time range of -780 s to 780 s.

## 4.3 Model

### 4.3.1 Analytic model

To interpret the observed oscillation patterns using the simple analytic solution, we consider the wave equation in the uniform vertical magnetic flux tube with a radius $R$. The trapped wave solution appears by choosing the exponentially decaying solution outside the flux tube in cylindrical coordinates (Edwin & Roberts 1983; Roberts 2019),

$$v_z = AJ_m(k_r r)\exp i\,(k_z z + m\theta - \omega t), \quad 0 \leq x < R \tag{4.1}$$

where the $v_z$ is the velocity fluctuation along the magnetic field, $A$ is an amplitude constant, $J_m$ is the first kind of the Bessel function of an azimuthal mode $m$, $\omega$ is the angular frequency, and $k_z$ is the vertical wavenumber. Here the azimuthal mode $m$ has an integer value. The $k_r$ is the radial wavenumber given as

$$k_r^2 = -\frac{(k_z^2 c_s^2 - \omega^2)(k_z^2 v_A^2 - \omega^2)}{(c_s^2 + v_A^2)(k_z^2 c_T^2 - \omega^2)} \tag{4.2}$$

where, $v_A$ is the Alfvén speed, $c_s$ is the sound speed and $c_T$ is the tube speed defined as $c_T^2 = \frac{c_s^2 v_A^2}{c_s^2 + v_A^2}$. Since observed oscillations have the nature of body waves, the $k_r^2$ should be positive.

The continuity of the total pressure and the radial velocity fluctuation at the boundary ($r = R$) gives a dispersion relation described as (Edwin & Roberts 1983),

$$\frac{1}{\rho_e(k_z^2 v_{A,e}^2 - \omega^2)} k_{r,e} \frac{K_m'(k_{r,e}R)}{K_m(k_{r,e}R)} = \frac{1}{\rho_0(k_z^2 v_A^2 - \omega^2)} k_r \frac{J_m'(k_r R)}{J_m(k_r R)} \tag{4.3}$$

where $\rho_0$ is the density, $K_m$ is the second kind of the modified Bessel function, the dash($\prime$) denotes the derivative of the Bessel function, and parameters with a subscript $e$ stand for the external region, $r > R$. For zero-external density limit, this relation is satisfied when $J_m(k_r R) \simeq 0$, and there are several $k_r$ satisfying this condition. Here we define the radial mode $n$ as the number of nodes $(J_m(k_r r) = 0)$ in the region $0 < r \leq R$. The radial mode $n$ has a positive integer value.

Note, the zero-external density limit is not the general case in the subphotosphere of the sunspot, but we can easily understand the physics between the slow body waves and the fast body waves in this limit because the equation can be easily described analytically by only considering the internal atmospheric condition ($c_s$ and $v_A$). In addition, the difference between the zero-external density limit and the numerical solution of the dispersion relation is small (see Figure 4.4).

Each resonance mode can have different amplitude $A_{m,n}$, orientation $\theta_m$, wavenumber $k_{r;m,n}$, $k_{z;m,n}$ and the phase $t_{m,n}$. Since several modes can be excited simultaneously, the vertical velocity fluctuation is the form,

$$\begin{aligned} v_z &= \sum_{m,n} v_{z;m,n} && (4.4) \\ &= \sum_{m,n} A_{m,n} J_m(k_{r;m,n} r) \exp i[k_{z;m,n} z + m(\theta - \theta_m) - \omega(t - t_{m,n})]. && (4.5) \end{aligned}$$

Here $\theta_0 = 0$ because $m = 0$ is the axisymmetric mode, and we set $t_{0,1} = 0$ as a reference. In the subphotospheric region, vertical wavenumber $k_{z;m,n}$ depends on modes because of the dispersion relation described in the subsequent section.

### 4.3.2 Cutoff wavenumber

The trapped waves are dispersive, and the wavenumber of each mode is obtained from the equation 4.2. In the special case of very low external density limit, the boundary condition in equation 4.3 leads to the simpler one: $J_m(k_r R) \simeq 0$, then the dispersion relation is described simply from the equation 4.2,

$$k^2_{z,\mp} = \frac{-b \pm \sqrt{b^2 - 4ac}}{2a}, \qquad (4.6)$$

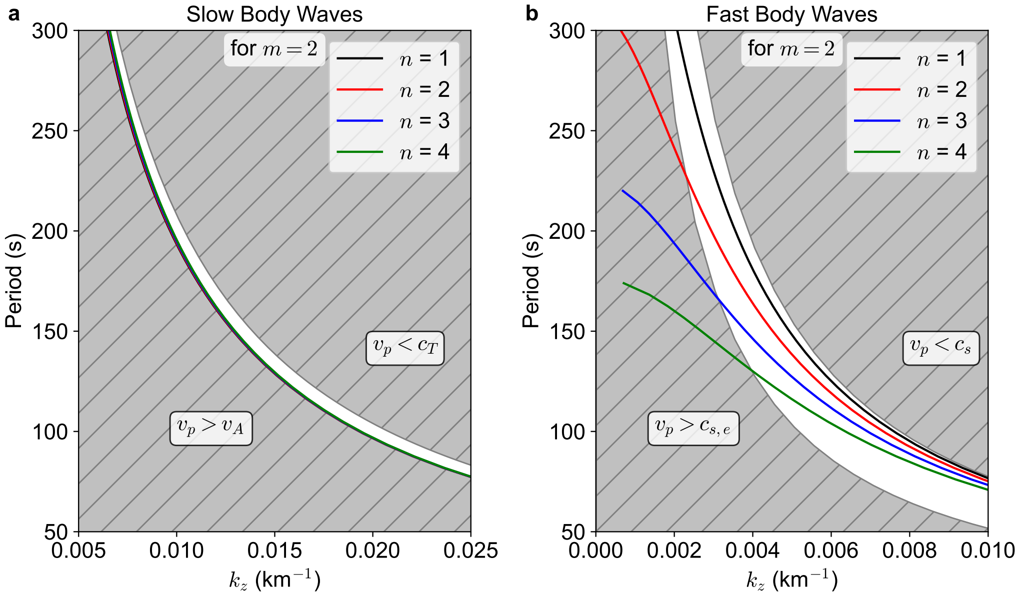

Figure 4.3 $p - k$ **diagrams. a** Period $p$ as a function of the vertical wavenumber $k_z$ of four radial modes of $m = 2$ azimuthal mode for the case of the slow body waves in the subphotospheric condition ($c_{s,e} > c_s > v_A$). **b** $p - k$ diagram for the case of the fast body waves. The white area in panel **a** marks the range of $v_A > v_p > c_T$ where the slow body wave solution can exist. The white area in panel **b** represents the range where the fast body wave solution can exist ($c_{s,e} > v_p > c_s$). We have taken the internal sound speed of $c_s = 8.1$ km s$^{-1}$, internal Alfvén speed of $v_A = 0.4c_s$, external sound speed of $c_{s,e} = 1.5c_s$, external Alfvén speed of $v_{A,e} = 0.5c_s$, and the tube speed of $c_T^2 = c_s^2 v_A^2/(c_s^2 + v_A^2)$. Here $v_p$ represents the longitudinal phase speed of waves, i.e. $v_p = \omega/k_z$.

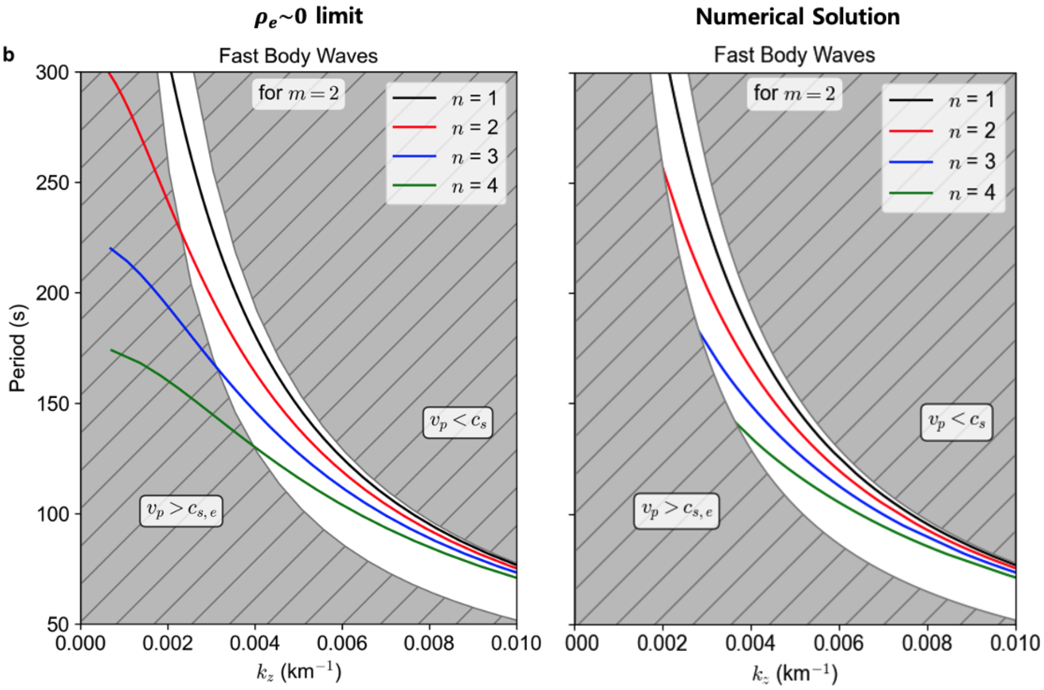

Figure 4.4 **Dispersion relations of the zero-external density limit and the numerical solution.** The left panel shows the dispersion relation of the fast body wave in the zero-external density limit shown in panel b of Figure 4.3. The right panel shows the numerical solution of the equation 4.3. In the numerical solution, wave mode in the gray area cannot be calculated. Two panels show a similar trend with just a small difference.

where $k_{z,+}$ is the vertical wavenumber of fast waves and $k_{z,-}$ is the solution of slow waves. The constants are of the form

$$a = v_A^2 c_s^2 R^2, \tag{4.7}$$

$$b = (c_s^2 + v_A^2)(f_m^2(n)c_T^2 - R^2\omega^2), \tag{4.8}$$

$$c = R^2\omega^4 - f_m^2(n)\omega^2(c_s^2 + v_A^2), \tag{4.9}$$

where $f_m(n)$ is $n$-th root of the Bessel function, $J_m(f_m(n)) = 0$. Figure 4.3 shows oscillation period $p$ as a function of vertical wavenumber $k_z$ for two body wave cases following the dispersion relation in the subphotospheric condition ($c_{s,e} > c_s > v_A$) at 190 km depth below the equipartition layer, where $c_{s,e}$ is the external sound speed, $c_s$ is the internal sound speed and $v_A$ is the internal Alfvén speed. Here only four radial modes of $m = 2$ azimuthal mode are plotted. The internal sound speed is derived from the extrapolation of the Maltby M model (Maltby et al. 1986). The internal Alfvén speed is derived following the method described in Cho et al.(Cho & Chae 2020): after measuring the mean magnetic field strength of 1400 G magnetic strength from the Helioseismic and Magnetic Imager onboard the Solar Dynamics Observatory (SDO/HMI(Schou et al. 2012)) at 100 km height, the magnetic field strength in the deeper region by applying the vertical gradient of $-1$ G km$^{-1}$ (Borrero & Ichimoto 2011). For simplification, we set the external sound speed to $1.5c_s$ and the external Alfvén speed to $0.5c_s$. Since the phase speed of the fast body waves $v_{p,f}$ is in between the internal sound speed and the external sound speed ($c_{s,e} > v_{p,f} > c_s > v_A$), the solution is confined in the white region. The slow body waves are valid if the phase speed ($v_{p,s}$) is in between the Alfvén speed and the tube speed ($v_A > v_{p,s} > c_T$). Even if the exterior magnetic field is negligible ($v_{a,e} = 0$), two body waves can exist in the flux tube (Roberts 1981; Edwin & Roberts 1982).

The noticeable difference between the slow body wave resonance model and the fast body wave resonance model comes from whether the cutoff wavenumber, which is related to the incident angle to the interface, exists or not. For the case of slow body waves, there is no cutoff wavenumber, and hence infinite radial modes can exist in all period ranges (panel a). For the case of fast body waves, however, the finite number of radial mode can be survived by the effect of the cutoff wavenumber (panel b). Moreover, this cutoff wavenumber highly depends on the oscillation period. In the case of $m = 2$ azimuthal mode waves, only one radial mode appears at the period of 300 seconds, three radial modes exist at the period of 150 seconds, and more than four radial modes can be survived at the period of 75 seconds.

## 4.4 Results

To reproduce the temporal evolution of the spatially and temporally filtered SWPs (Figure 4.5b), we found the free parameter values of $A_{m,n}$, $\theta_{m,n}$ and $t_{m,n}$ in the equation 4.5. The radial wavenumber $k_{r;m,n}$ is derived from the boundary condition, and we set $z = 0$. At first, we found the phase difference value $t_{m,n}$ from the shape of spiral arms and their temporal evolution. Second, we determined the amplitude $A_{m,n}$ from the apparent radial pattern speed and the width of the spiral arms. After that, we rotated the patterns to fit their orientation $\theta_m$ to the observation. The two-armed SWP was reconstructed by the superposition of nine resonant modes; three azimuthal modes ($m = 0, \pm 2$) and three radial modes ($n = 1, 2, 3$) of each azimuthal mode (Figure 4.1 d-e). The temporal evolution of the model is shown in the bottom panels of Figure 4.5, and the model parameters are described in Table 4.1. The temporal evolutions of $m = 0$ and $m = 2$ azimuthal modes are shown in Figure 4.6 and 4.7, respectively. During the lifetime of the SWPs, the model parameters and the number of resonant modes are not changed.

The shape of spiral patterns is relevant to the phase difference ($t_{m,n}$) between radial modes. The inner region of the patterns is highly affected by high-order radial modes, and the outer part is associated with low-order modes. The phase speed

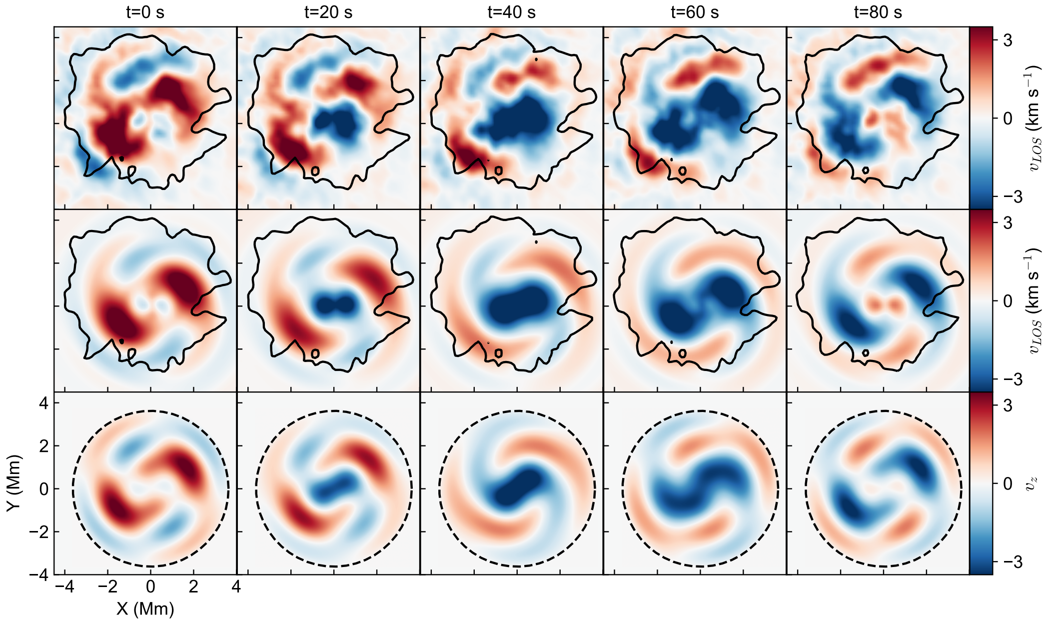

Figure 4.5 **Temporal evolution of the spiral-shaped wave patterns.** Top row: Observed Doppler velocity maps temporally filtered in the frequency range of $5.5-9$ mHz. Middle row: Doppler velocity maps that are temporally filtered in the same frequency range and are spatially filtered in the azimuthal mode $m = 0$, and 2. Bottom row: Modeled LOS velocity fluctuation $v_z$ constructed by the superposition of total nine resonance modes; $m = 0, \pm 2$, and $n = 1, 2, 3$. Columns show the temporal evolution of each map from left to right. The time $t = 0$ is equal to 17:43:27 UT. The black contour indicates the boundary of the pore, and the black dashed circle represents the boundary of the flux tube of the model. The oscillation period of the patterns is about 160 seconds, and input model parameters are shown in Table 4.1. Temporal evolutions of $m = 0$ and 2 modes are illustrated in Figure 4.6 and 4.7 respectively.

Table 4.1 Input parameters of the model shown in Figure 4.5

| $m$ | $n$ | $A_{m,n}$ (km s$^{-1}$) | $\theta_m$ ($^\circ$) | $t_{m,n}$ (s) |
|---|---|---|---|---|
| 0 | 1 | 1.50 | 0 | 0 |
| 0 | 2 | 2.25 | 0 | -20 |
| 0 | 3 | 1.50 | 0 | -40 |
| 2 | 1 | 2.00 | 30 | 28 |
| 2 | 2 | 3.00 | 30 | -2 |
| 2 | 3 | 3.00 | 30 | -52 |
| -2 | 1 | 0.60 | 30 | 28 |
| -2 | 2 | 0.90 | 30 | -2 |
| -2 | 3 | 0.90 | 30 | -52 |

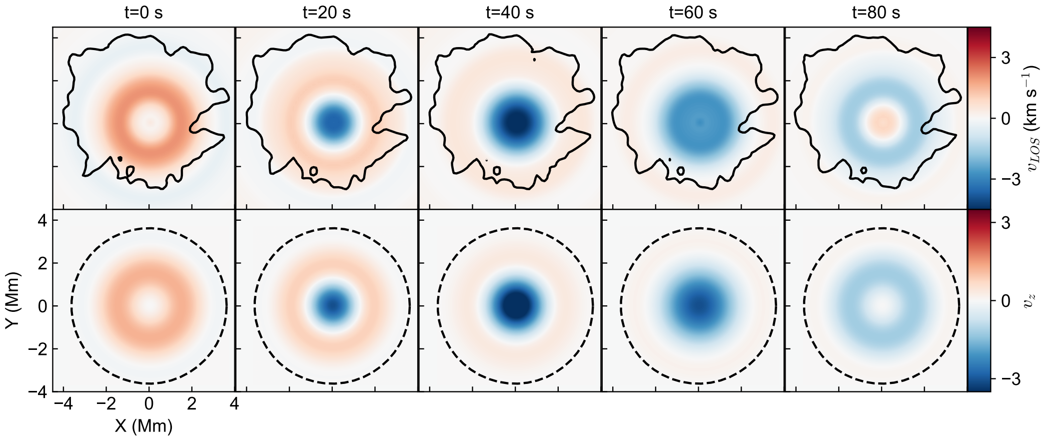

Figure 4.6 **Temporal evolution of oscillation patterns filtered in $m = 0$ mode.** Top row: Similar to the middle row in Fig 4.5 but filtered in the azimuthal mode $m = 0$. Bottom row: Modeled LOS velocity fluctuation of $m = 0$ mode.

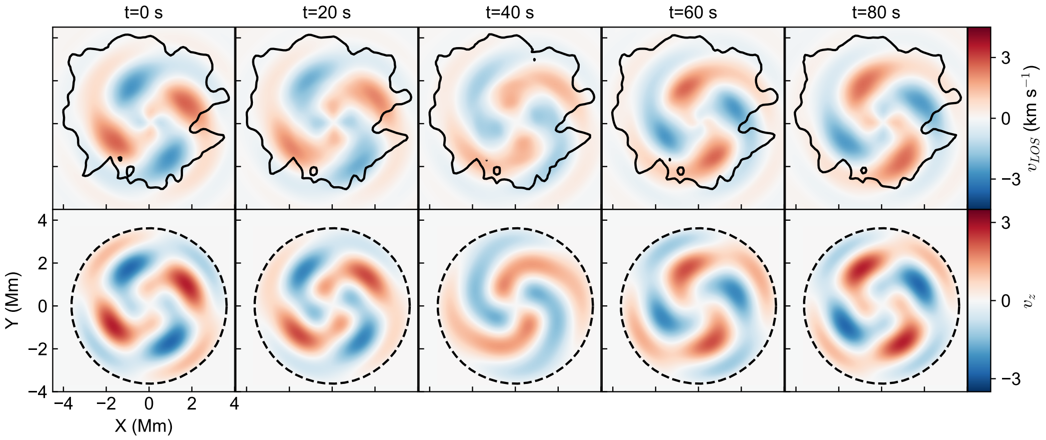

Figure 4.7 **Temporal evolution of oscillation patterns filtered in $m = 2$ mode.** Top row: Similar to the middle row in Fig 4.5 but filtered in the azimuthal mode $m = 2$. Bottom row: Modeled LOS velocity fluctuation of $m = \pm 2$ mode.

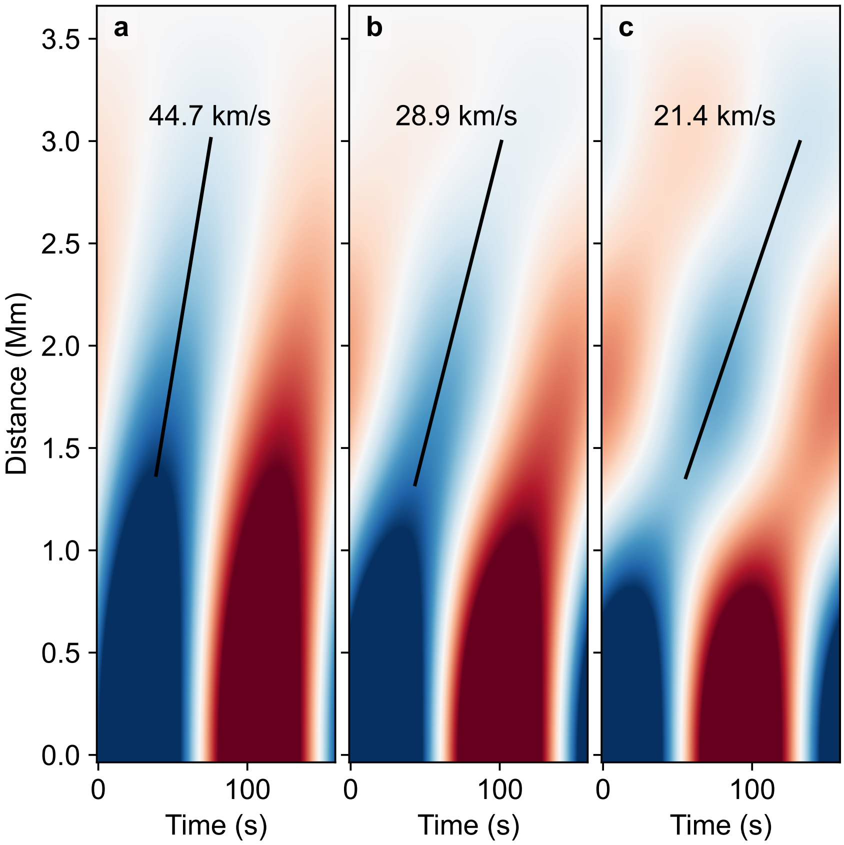

Figure 4.8 **Time-distance map of modeled m=0 waves. a** Time-distance (TD) map of the $m = 0$ mode with the amplitudes of $A_{0,1} = 2.25$, $A_{0,2} = 2.0$ and $A_{0,3} = 0.5$. **b** TD map with the amplitudes of $A_{0,1} = 1.5$, $A_{0,2} = 2.25$ and $A_{0,3} = 1.5$. **c** TD map with the amplitudes of $A_{0,1} = 0.5$, $A_{0,2} = 2.0$ and $A_{0,3} = 2.25$. All of them have the phase differences of $t_{0,1} = 0$, $t_{0,2} = -20$ and $t_{0,3} = -40$. The solid lines represent the gradient of ridges.

difference may be responsible for the phase difference because it takes different times for different modes to establish standing waves after being reflected at the flux tube boundary. If the high-order modes form the standing waves earlier than the low-order modes for non-zero azimuthal modes, the inner part appears to rotate earlier than the outer part. As a result, the superposition of radial wave modes with different phases forms trailing spiral arm structures.

The speed of radial apparent fast-moving patterns is associated with the amplitude ratio between radial modes (see Figure 4.8). If the $n = 1$ mode has the dominant wave power of the patterns, the radial pattern speed becomes faster (panel a). On the other hand, if the $n = 2$ or 3 has the most of the wave power of the patterns, the apparent speed becomes slower (panels b and c). Therefore, the speed of the radial moving patterns may be irrelevant to the depth of a source suggested in the previous studies (Zhao et al. 2015; Cho & Chae 2020; Felipe & Khomenko 2017), but it corresponds to the energy distribution between radial modes.

The effect of the cutoff wavenumber is shown in the observation of the $m = 2$ azimuthal mode filtered in three different frequency band (Figure 4.9). The $2.5 - 4$ mHz ($4.2 - 6.7$ minute) frequency-filtered Doppler velocity map shows the blob patterns generated by only one radial mode (panel a). In contrast with the low frequency-filtered map, the oscillation pattern filtered in the range of $5.5 - 9$ mHz ($1.9 - 3.0$ minute) forms the spiral arms associated with the three radial modes (panel b), and more winding spiral structures are shown in the $12 - 20$ mHz ($0.8 - 1.4$ minute) frequency-filtered map because of the superposition of more than four radial modes (panel c). These support the idea that the observed chromospheric features are originally generated by the resonance of the fast body waves in the subphotosphere.

The cutoff wavenumber also depends on the size of a flux tube (see equations (4.6)-(4.9)). If the flux size is less than 2 Mm, only one resonance mode, fundamental sausage mode ($m = 0$, $n = 1$), can be trapped in the flux tube. For the intermediate

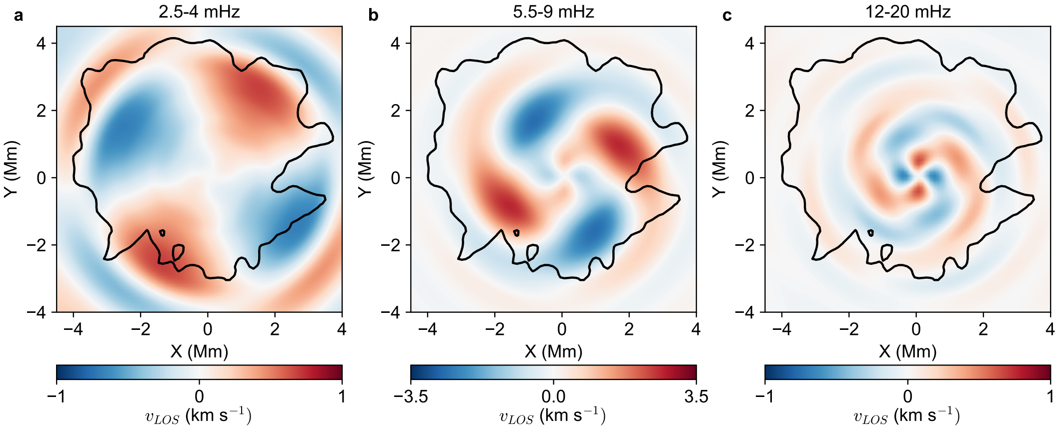

Figure 4.9 **Oscillation patterns filtered in three different frequency bands.** **a** Observed Doppler velocity map filtered in the range of 2.5 – 4 mHz. **b** Velocity map filtered in the range of 5.5 – 9 mHz. **c** Velocity map filtered in the range of 12 – 20 mHz. The black contour represents the boundary of the pore.

size of the flux tube with the size of 7 Mm, the waves have the maximum order of radial mode of four with $m = 0$ and the highest azimuthal mode of eight with $n = 1$. However, a large-scale sunspot of more than 30 Mm can trap many resonance modes, so it is hard to distinguish whether these modes occur from the resonance of the slow waves or the resonance of the fast waves. Therefore, only sausage or kink body waves have been reported previously in small-scale flux tubes such as pores (Morton et al. 2011; Keys et al. 2018), the limited number of resonance modes have been detected in the intermediate sunspots (Kang et al. 2019; Albidah et al. 2022). and more than 30 resonance modes have been identified in large-scale sunspots (Stangalini et al. 2022).

## 4.5 Discussion

For the first time, we successfully reproduced the observed temporal evolution of the spiral-shaped wave patterns by the superposition of the resonance modes of the fast body waves driven in the subphotosphere. The spiral arms were constructed by the superposition of three radial modes of non-zero azimuthal modes, and the speed of the fast-moving radial pattern was associated with the energy distribution between the radial modes. Since the cutoff wavenumber of the fast body waves limited the high-order radial modes, only a few low-order radial modes were identified in the pore. The evidence of the cutoff wavenumber was detected in the filtered Doppler velocity maps in three different frequency ranges; 2.5−4 mHz, 5.5−9 mHz, and 12−20 mHz. The existence of the cutoff wavenumber is the most remarkable difference from the solution of trapped slow body waves.

How can the resonance of the fast body waves contribute to the chromospheric oscillations of slow waves? The mode conversion at the equipartition layer ($c_s = v_A$) links the subphotospheric fast waves to the chromospheric slow waves (Zhugzhda & Dzhalilov 1984; Cally 2001; Schunker & Cally 2006; Cally 2007) (see Figure 4.10).

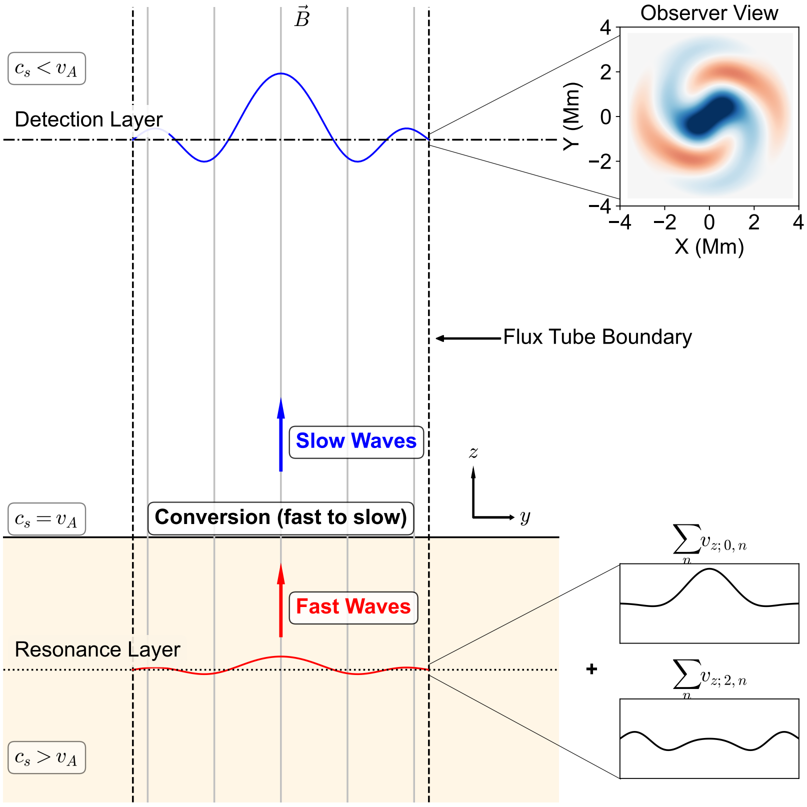

Figure 4.10 **Schematics of the vertical cross-section view of the model.** The yellow area represents the region where the sound speed is faster than the Alfvén speed ($c_s > v_A$), and the white area represents the region where the sound speed is slower than the Alfvén speed ($c_s < v_A$). The black solid line between the two regions represents the equipartition layer ($c_s = v_A$) where the mode conversion can occur. The gray vertical lines represent the magnetic field lines, and the vertical dashed line illustrates the boundary of the flux tube. The red line demonstrates the vertical velocity fluctuation $v_z$ of fast body waves and the blue line illustrates the $v_z$ of slow body waves. The dotted horizontal line indicates the resonance layer of the fast body waves, and the dash-dotted horizontal line expresses the detection layer. The two panels shown in the right-bottom corner illustrate the vertical velocity fluctuation of two azimuthal modes of $m = 0$ and 2. The right-top panel shows the horizontal cross-section view of the modeled oscillation patterns shown in panel d of Figure 4.1.

First, the resonance of fast body waves occurs at the resonance layer in the subphotosphere ($c_s > v_A$). When the waves propagate upwards through the equipartition layer ($c_s = v_A$), some portion of fast waves is converted to slow waves maintaining their oscillation patterns. After mode conversion, the slow waves propagate upwards along the vertical magnetic field. Therefore we can observe inherited oscillation patterns of the resonance of the fast body waves even in the detection layer of the chromosphere ($c_s < v_A$).

The mode conversion efficiency depends on the order of the radial mode. In other words, the shape of oscillation patterns in the subphotospheric region may be slightly different from the patterns observed in the chromosphere. The direction of the wave vector or the ratio of the vertical wavenumber $k_z$ to the radial wavenumber $k_r$ depends on the order of the radial mode. For the lowest order radial mode ($n = 1$), the $k_z/k_r$ becomes 3, but the highest order radial mode of $n = 3$ has a low wavenumber ratio of around 1. Since the fast-to-slow mode conversion is enhanced when the wave vector is aligned with the field lines (Schunker & Cally 2006), more energy of the fast waves of the low-order modes can be converted to the slow waves rather than the high-order modes. As a result, the chromospheric oscillation patterns have a larger amplitude ratio of the low-order to high-order modes than the patterns in the subphotosphere. Thus the chromospheric oscillation patterns can show faster radial apparent pattern speed than the subphotospheric patterns according to the notion shown in Figure 4.8. In this chapter, we have ignored this modal-dependant transmission to describe the observed patterns analytically, but in a further study, we will consider this effect numerically.

There is a physical reason why horizontal resonance occurs in fast waves, not in slow waves. To form trapped oscillation patterns in the horizontal plane, waves should propagate energy across the field lines. Since the wave vector and group velocity of the slow waves are highly aligned with the field line even in the subphotospheric region, the slow waves propagate upwards before being trapped in the flux tube. For the case of fast waves, however, the vertical wavenumber is comparable to the radial wavenumber, so it is relatively easier for the fast waves to propagate the wave energy across the field line rather than the slow waves. Therefore, fast waves are preferred to for the horizontal resonance in flux tubes.

The driving sources of the oscillation patterns can be either internal magneto-convection or external p-mode. Regardless of the location of a source, the oscillations can show similar patterns if the waves are trapped in the flux tube. In this regard, the wave source does not need to be located at the center of the oscillation patterns. The center of oscillation patterns is related to the shape of the flux tube. In an axisymmetric circular sunspot, the center of oscillation patterns is located at the center of the flux tube, and the central position of the resonances in an irregular-shaped sunspot is affected by the field geometry (Albidah et al. 2022). Therefore, one should be careful to determine the source of waves from the apparent motion of the oscillation patterns.

The solution of fast body waves exists only in a shallow range of the subphotosphere ($c_{s,e} > c_s > v_A$). In the deep region below the surface, the effect of the magnetic field is negligible, and then it is difficult to trap the waves in the flux tube because the boundary becomes ambiguous ($c_s \sim c_{s,e}$). If the internal sound speed is slow enough near the equipartition layer, more than four radial modes can be trapped in the observed pore for the case of 3-minute waves, but it is inconsistent with the observation. Thus the fast wave resonance should occur in a confined layer. Calculating the depth of the resonance layer using the Maltby sunspot M model (Maltby et al. 1986), the fast body wave resonance of the observed two-armed SWPs is formed in a shallow range of -250 km to -110 km below the equipartition layer that equals $4 < \beta < 10$ in terms of plasma beta.

Our research sheds light on the physical nature and origin of umbral oscillations and contributes to the establishment of the subphotospheric seismology in the magnetic flux tube. Since the cutoff wavenumber depends on the internal/external sound speed and internal Alfvén speed for a given flux tube size and oscillation frequency, we can derive the atmospheric condition from the chromospheric oscillation patterns by using this model. Our study is significant in that we can infer the atmospheric conditions and the wave phenomena in the unobservable subphotosphere through the observable oscillation patterns in the chromosphere.

# Chapter 5

# Summary and Discussion

## 5.1 Summary

In this thesis, we investigated the nature and origin of two-dimensional oscillation patterns in sunspot umbrae by comparing the observations and models.

In Chapter 2, we reproduced observed one- and two-armed spiral-shaped wave patterns in the pore using the internal excitation model. According to this model, the spiral arms may be generated by the non-zero azimuthal mode of a localized source beneath the photosphere. The number of spiral arms is the same as the magnitude of the azimuthal mode, and the rotation direction is determined by its sign. In this model, the radial moving patterns and the spiral shape may be associated with the depth of the disturbance. From this relation, we derived that the source of the observed SWPs may be located at a depth of 1600 km below the photospheric surface.

In Chapter 3, we investigated the statistical properties of 241 spiral-shaped wave patterns in sunspot umbrae. The detection probability of 0.24 per hour is lower than our expectation. This low detection rate implies that there may be non-rotating patterns of non-axisymmetric mode with the balanced opposite sign of azimuthal modes; $+m$ and $-m$. The oscillation period of 150 seconds and the lifetime of 780 seconds are comparable to conventional umbral oscillations. The rotation direction is independent of the hemisphere and the magnetic twist. It implies that SWPs may be generated by the local turbulent motions if they originated from an internal source. We indirectly inferred that the source of SWPs is between 2 Mm and 10 Mm below the equipartition layer using the apparent radial speed supposing the waves are excited by the interior motion.

In Chapter **??**, we proposed the subphotospheric fast resonance model that more precisely reproduces the observed chromospheric patterns of umbral oscillations. This model is contrasted with the former internal excitation model employed in the works described in the previous chapters. In this chapter, we have corrected the analytic solution of the former model by considering the boundary effect of the flux tube. In addition, we have interpreted the two-dimensional patterns in three different frequency bands as the effect of the cutoff wavenumber or cutoff radial mode related to the incident angle of each radial mode. According to this new model, the chromospheric patterns of umbral (slow) waves are regarded as the inherited patterns of the resonance of fast waves in the subphotosphere. Either internal convective motion or external p-mode waves in the subphotosphere can generate the proposed resonance of fast waves. The observed patterns in a pore are formed within narrow and shallow layers between -250 km to -110 km below the surface.

The differences between the earlier internal excitation model (IEM) and the later subphotospheric fast resonance model (SFRM) are described in Figure 5.1. The SFRM can reproduce spatial details of the patterns of umbral oscillations because of the existence of the radial mode. Furthermore, the frequency dependence of the oscillation patterns can be interpreted as the effect of the cutoff wavenumber (or cutoff radial mode) in the SFRM. The source of the pattern in the IEM is the localized random impulsive events. Accordingly, the oscillation pattern can be

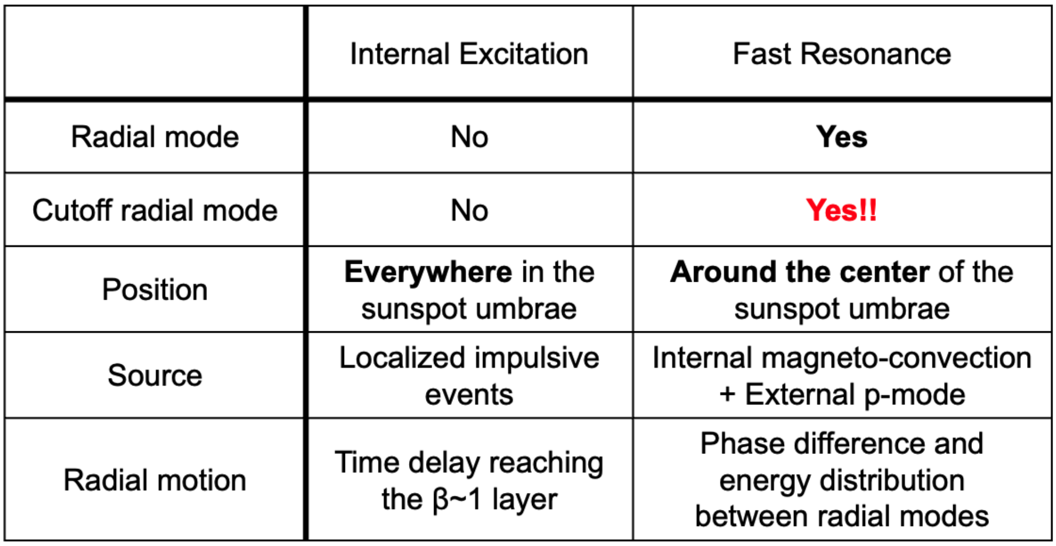

| | Internal Excitation | Fast Resonance |
|---|---|---|
| Radial mode | No | **Yes** |
| Cutoff radial mode | No | **Yes!!** |
| Position | **Everywhere** in the sunspot umbrae | **Around the center** of the sunspot umbrae |
| Source | Localized impulsive events | Internal magneto-convection + External p-mode |
| Radial motion | Time delay reaching the β~1 layer | Phase difference and energy distribution between radial modes |

Figiure 5.1 Summary of the internal excitaiton model and the subphotospheric fast resonance model.

located everywhere in the umbrae. On the other hand, the source of the SFRM can be either internal excitation or the external p-mode. For that reason, the SFRM can propagate more energy to the upper atmosphere. In addition, the wave pattern of the SFRM can be located near the center of the umbrae because it is formed by the standing waves trapped in the flux tube. In the IEM, the apparent radially propagating pattern is related to the depth of the source. By contrast, in the SFRM, the radial propagation is associated with the phase difference and the energy distribution between radial modes.

The remarkable achievement of our studies is that the observed umbral slow waves are originally fast waves below the surface. The key process connecting these two wave modes is the mode conversion at the equipartition layer. With the help of this process, sunspots can transfer the energy of the solar interior to the upper atmosphere with the two linked magnetoacoustic waves of acoustic nature. Moreover, we can explore the unobservable sunspot interior from the umbral oscillations with devised models. If we improve these models more quantitatively with the help of numerical simulation, we can find a hint to solve the coronal heating problems.

## 5.2 Future works

Our results broaden our understanding of the observed oscillation in the magnetized region. Based on this knowledge, we suggest several research subjects. In this section, we introduce several ideas and some preliminary results.

### 1. Detection of non-rotating patterns of umbral oscillations

As discussed in Chapter 3, the low detection rate of SWPs implies that there should be non-rotating patterns (NRPs) of umbral oscillation. We identified some cases of NRPs in a pore observed on June 24, 2018, from 18:36 to 20:34 UT (Figure 5.2).

The first case shows the NRP with the dominant powers at the azimuthal numbers 0 and 2, and the second case is the NRP of the superposition of $m = 0$ and 3. We reproduced the observed patterns using the temporal evolution of NRPs and the time-distance map. The apparent radial speeds of $m = 0$ and $m = 2$ are different (Figure 5.3 a and b). It supports the idea of the subphotospheric fast resonance model because the radial speeds of the different modes are the same if two modes are generated simultaneously by a single local disturbance, as suggested in the internal excitation model. The second important finding is that the oscillation power is also horizontally distributed regardless of the local magneto-convection shown in the photosphere (Figure 5.3 c and f). Therefore, it should be careful to identify the source of the slow waves from the distribution of the oscillation power.

### 2. Nature of penumbral waves

What about the waves shown in the penumbral? According to the subphotospheric model, the penumbral waves can also be related to the trapped umbral waves. If the penumbral waves are related to the subphotospheric model, the penumbral waves are linked with the patterns of umbral oscillations. To find this feature, we analyzed sunspot waves temporally filtered in the period range of 3-minute and 5-minute bands, respectively. We find that either 3-minute waves or 5-minute waves appear to propagate from the umbra to the penumbra (Figure 5.4). From this result, we conjecture that the penumbral waves may be related to the leaky waves. After improving the analytic model, we will reproduce the observation.

### 3. Surface waves at the umbra-penumbra boundary and their relation to the Alfvénic waves

As mentioned in Chapter 1, the surface wave can exist near the umbra-penumbra boundary. If these surface waves are generated in the subphotosphere like the body

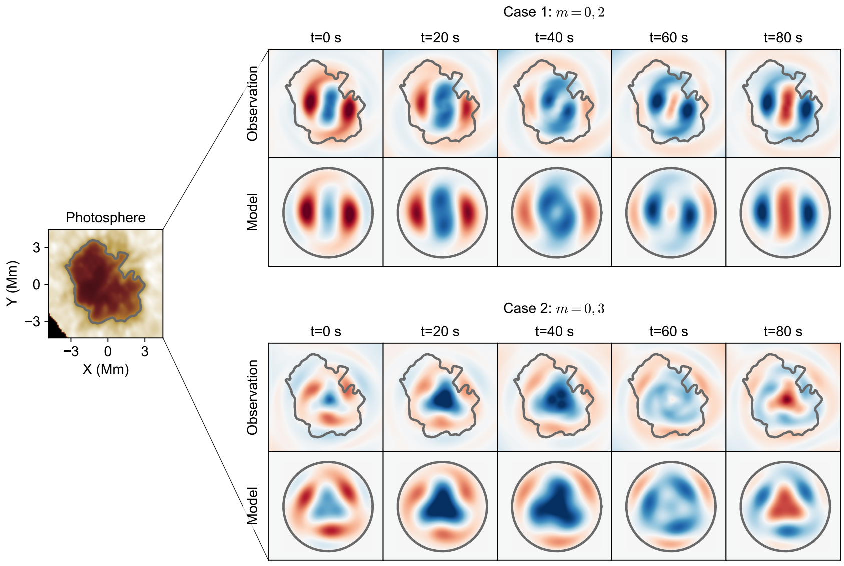

Figiure 5.2 Example of non-rotating patterns. (Left) Photospheric intensity image of the pore observed on June 24, 2018, from 18:36 19:51 UT using GST/FISS. (Right 1st column) Chromospheric LOS velocity map temporally filtered in the frequency range from 5 to 9 mHz and spatially filtered in the frequency range at $m$=0 and 2, observed at 19:12 UT. (Right 2nd column) Modeled velocity map with ten eigenmodes. (Right 3rd column) Same with the 1st column but spatially filtered in the frequency range at $m$=0 and 3, observed at 20:23 UT. (Right 4th column) Model of observed NRP with ten eigenmodes.

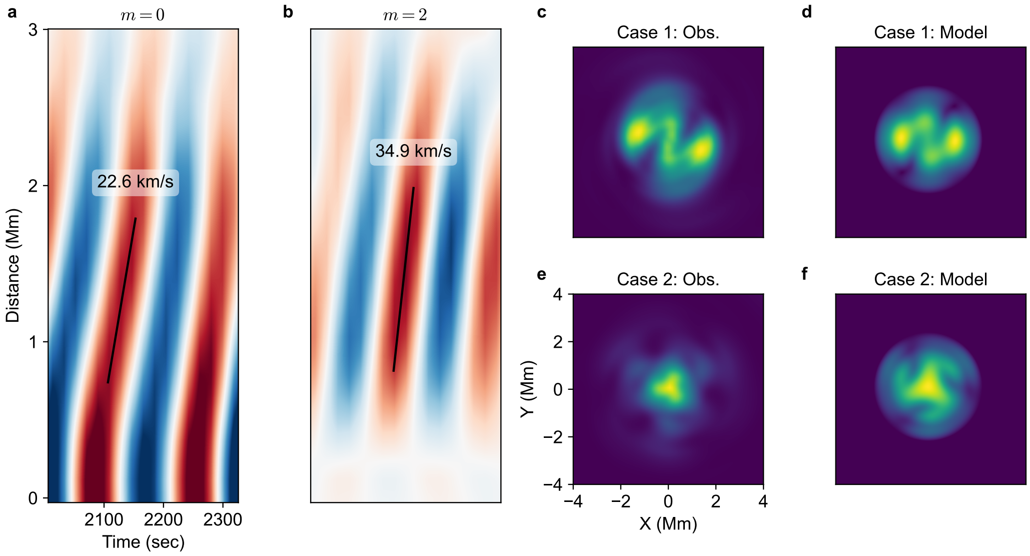

Figiure 5.3 Time-distance map and power map of NRPs. **a** Time-distance map of case 1 spatially filtered for $m = 0$ mode. **b** Time-distance map of case 1 spatially filtered for $m = 2$ mode. **c** Power map of case 1 (observation). **d** Power map of case 1 (model). **e** Power map of case 2 (observation). **f** Power map of case 2 (model).

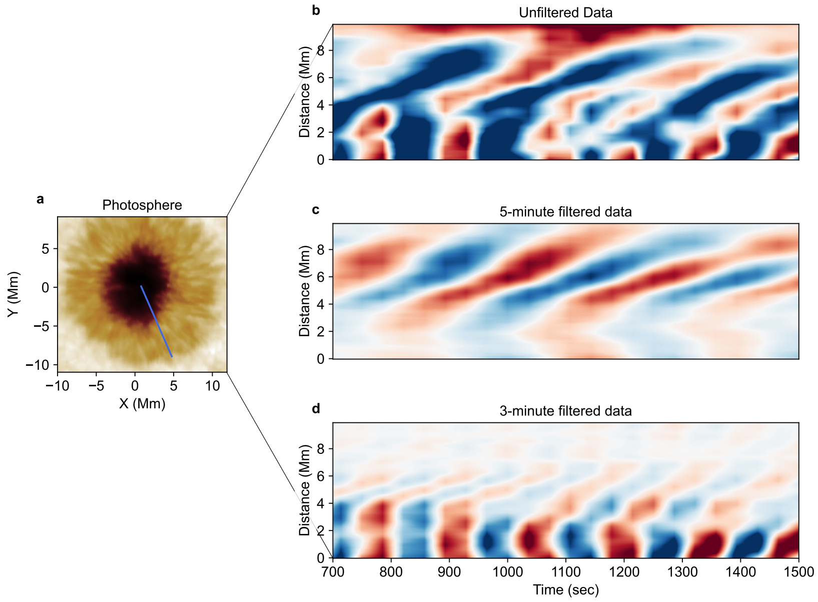

Figiure 5.4 Time-distance map of penumbral waves. **a** Photospheric intensity image of a sunspot observed at 2013-07-28 22:15 UT. **b** Time-distance map of unfiltered LOS velocity map along the blue slit shown in the panel **a**. **c** Time-distance map filtered in the 5-minute band. **d** Time-distance map filtered in the 3-minute band.

waves, the only allowable solution is the slow surface waves (see Figure 6 of Edwin & Roberts (1983)). If we decompose the patterns of body waves with the subphotospheric fast resonance model, we can identify the surface waves at the umbra-penumbra boundary. Moreover, slow waves have magnetic nature in the high-$\beta$ region, and the slow waves are strongly coupled with Alfvén waves. In this region, a portion of slow waves can be converted to the Alfvén waves, maintaining their magnetic nature (Cally 2022). Therefore, surface waves can transfer the magnetic energy of the solar interior to the upper atmosphere.

### 4. Sunspot seismology

In helioseismology, $p$-mode waves can be described by spherical harmonics, and this harmonic feature can be identified in the $k-\omega$ diagram. Similarly, umbral oscillations can be given by cylindrical harmonics using the resonance model. Thus the harmonic feature of umbral oscillation can also be detected in the $k-\omega$ diagram in a sunspot umbra with enough spatial and temporal size and resolution. According to Figure 4.3, the separation between two harmonic branches is about 20 seconds in time and about 200 km in space for 3-minute waves. Considering the Nyquist frequency, the temporal resolution should be better than 10 seconds, and the spatial resolution should be better than 100 km. This resolution is slightly better than the resolution of the FISS. If we improve the FISS in the near future, we can resolve this harmonic feature in the frequency domain.

### 5. Distribution of oscillation period in sunspot umbrae

The distribution of the predominant oscillation period is different even in an umbra. The oscillation period near the umbra center is shorter than the outer parts. Conventionally this observed phenomenon is considered as the difference of acoustic cutoff by the effective gravity of inclination of the magnetic field (Reznikova et al.

2012; Jess et al. 2013). This phenomenon can also be interpreted as the effect of the distribution of the maximum amplitude of each radial mode (see Figure 4.9). Therefore, we will compare these two scenarios by comparing the oscillation power map and the magnetic field inclination map.

### 6. Relation between oscillation patterns and structure of sunspot

The morphological patterns of umbral oscillations may depend on the size and structure of sunspots. According to equation (4.6-4.9), the cutoff wavenumber of trapped fast waves in the subphotosphere depends on the size of the flux tube. The larger the umbra is, the more radial modes can be trapped in the umbra. Thus, the shape of oscillation patterns may depend on the size of the flux tube. Moreover, the oscillation patterns are affected by the shape of the sunspots. If the sunspots have an elliptical shape, the oscillation patterns are elongated along the major axis (Aldhafeeri et al. 2021). Therefore, we should consider the structure of the sunspots to derive the wave mode correctly.

### 7. Oscillation patterns in fragmented sunspots.

Sunspots can be fragmented by the magneto-convection, such as a light bridge. Each separated sunspot can trap the waves. If the flow in the light bridge disturbs these two sunspots, wave patterns in two separated sunspots may be similar or rotate in opposite directions. If we find these features, the results also support the idea of a subphotospheric fast resonance model because the internal source cannot simultaneously disturb two separated flux tubes.

### 8. Energy transfer of the oscillation patterns

According to the fast subphotospheric resonance model, the external p-mode waves can be absorbed by a sunspot, and absorbed energy can be transferred to the corona along the magnetic field. In this model, the sunspot acts as an optical fiber that traps the energy within the tube and transfers this energy to the opposite end. If we quantitatively measure the absorbed energy of $p$-mode in the sunspot and the energy flux of the waves, we can give a clue to the coronal heating problem.

In this dissertation, we have successfully explained the chromospheric oscillation patterns based on the mode of fast wave resonance in the subphotosphere. We expect that our model can give a hint or clue to the unsolved problems associated with sunspot waves, such as the origin of Alfvénic waves or the chromospheric heating problem.

# Bibliography

Albidah, A. B., Fedun, V., Aldhafeeri, A. A., et al. 2022, ApJ, 927, 201

Aldhafeeri, A. A., Verth, G., Brevis, W., et al. 2021, ApJ, 912, 50

Alfvén, H. 1942, Nature, 150, 405

Anderson, T. W., & Darling, D. A. 1952, The annals of mathematical statistics, 193

Aschwanden, M. J., Fletcher, L., Schrijver, C. J., & Alexander, D. 1999, ApJ, 520, 880

Beckers, J. M., & Schultz, R. B. 1972, Sol. Phys., 27, 61

Beckers, J. M., & Tallant, P. E. 1969, Sol. Phys., 7, 351

Bhatnagar, A., Livingston, W. C., & Harvey, J. W. 1972, Sol. Phys., 27, 80

Bloomfield, D. S., Lagg, A., & Solanki, S. K. 2007, ApJ, 671, 1005

Borrero, J. M., & Ichimoto, K. 2011, Living Reviews in Solar Physics, 8, 4

Bunte, M., & Bogdan, T. J. 1994, A&A, 283, 642

Cally, P. S. 2001, ApJ, 548, 473

Cally, P. S. 2007, Astronomische Nachrichten, 328, 286

Cally, P. S. 2022, MNRAS, 510, 1093

Cally, P. S., & Bogdan, T. J. 1997, ApJL, 486, L67

Cally, P. S., Bogdan, T. J., & Zweibel, E. G. 1994, ApJ, 437, 505

Cally, P. S., Crouch, A. D., & Braun, D. C. 2003, MNRAS, 346, 381

Cao, W., Gorceix, N., Coulter, R., et al. 2010, Astronomische Nachrichten, 331, 636

Centeno, R., Collados, M., & Trujillo Bueno, J. 2006, ApJ, 640, 1153

Chae, J., Cho, K., Lim, E.-K., & Kang, J. 2022, ApJ, 933, 108

Chae, J., & Goode, P. R. 2015, ApJ, 808, 118

Chae, J., Kang, J., & Litvinenko, Y. E. 2019, ApJ, 883, 72

Chae, J., Lee, J., Cho, K., et al. 2017, ApJ, 836, 18

Chae, J., Lim, E.-K., Lee, K., et al. 2023, ApJL, 944, L52

Chae, J., & Litvinenko, Y. E. 2018, ApJ, 869, 36

Chae, J., Park, H.-M., Ahn, K., et al. 2013a, Sol. Phys., 288, 89

Chae, J., Song, D., Seo, M., et al. 2015, ApJL, 805, L21

Chae, J., Yang, H., Park, H., et al. 2014, ApJ, 789, 108

Chae, J., Park, H.-M., Ahn, K., et al. 2013b, Sol. Phys., 288, 1

Cho, K., & Chae, J. 2020, ApJL, 892, L31

Cho, K., Chae, J., Lim, E.-k., & Yang, H. 2019, ApJ, 879, 67

Cho, K., Chae, J., & Madjarska, M. S. 2021, A&A, 656, A86

De Moortel, I., Ireland, J., Hood, A. W., & Walsh, R. W. 2002, A&A, 387, L13

Deubner, F. L. 1975, A&A, 44, 371

Edwin, P. M., & Roberts, B. 1982, Sol. Phys., 76, 239

Edwin, P. M., & Roberts, B. 1983, Sol. Phys., 88, 179

Felipe, T., & Khomenko, E. 2017, A&A, 599, L2

Felipe, T., Khomenko, E., Collados, M., & Beck, C. 2010, ApJ, 722, 131

Felipe, T., Kuckein, C., Khomenko, E., & Thaler, I. 2019, A&A, 621, A43

Giovanelli, R. G. 1972, Sol. Phys., 27, 71

Goldreich, P., & Kumar, P. 1990, ApJ, 363, 694

Grant, S. D. T., Jess, D. B., Stangalini, M., et al. 2022, ApJ, 938, 143

Gurman, J. B., Leibacher, J. W., Shine, R. A., Woodgate, B. E., & Henze, W. 1982, ApJ, 253, 939

Jacoutot, L., Kosovichev, A. G., Wray, A., & Mansour, N. N. 2008, ApJL, 684, L51

Jess, D. B., De Moortel, I., Mathioudakis, M., et al. 2012, ApJ, 757, 160

Jess, D. B., Reznikova, V. E., Van Doorsselaere, T., Keys, P. H., & Mackay, D. H. 2013, ApJ, 779, 168

Jess, D. B., Van Doorsselaere, T., Verth, G., et al. 2017, ApJ, 842, 59

Kalkofen, W., Rossi, P., Bodo, G., & Massaglia, S. 1994, A&A, 284, 976

Kang, J., Chae, J., Nakariakov, V. M., et al. 2019, ApJL, 877, L9

Keys, P. H., Morton, R. J., Jess, D. B., et al. 2018, ApJ, 857, 28

Khomenko, E., & Cally, P. S. 2012, ApJ, 746, 68

Khomenko, E., & Collados, M. 2006, ApJ, 653, 739

Khomenko, E., & Collados, M. 2015, Living Reviews in Solar Physics, 12, 6

Kitiashvili, I. N., Kosovichev, A. G., Mansour, N. N., Wray, A. A., & Sandstrom, T. A. 2019, ApJ, 872, 34

Lee, J. W. 1993, ApJ, 404, 372

Lemen, J. R., Title, A. M., Akin, D. J., et al. 2012, Sol. Phys., 275, 17

Lites, B. W. 1984, ApJ, 277, 874

Löhner-Böttcher, J., & Bello González, N. 2015, A&A, 580, A53

López Ariste, A., Centeno, R., & Khomenko, E. 2016, A&A, 591, A63

Maltby, P., Avrett, E. H., Carlsson, M., et al. 1986, ApJ, 306, 284

Maltby, P., Brynildsen, N., Fredvik, T., Kjeldseth-Moe, O., & Wilhelm, K. 1999, Sol. Phys., 190, 437

Mihalas, D., & Mihalas, B. W. 1984, Foundations of radiation hydrodynamics (Oxford University Press)

Morton, R. J., Erdélyi, R., Jess, D. B., & Mathioudakis, M. 2011, ApJL, 729, L18

Morton, R. J., Verth, G., Jess, D. B., et al. 2012, Nature Communications, 3, 1315

Nakariakov, V. M., Ofman, L., Deluca, E. E., Roberts, B., & Davila, J. M. 1999, Science, 285, 862

Nakariakov, V. M., Anfinogentov, S. A., Antolin, P., et al. 2021, Space Sci. Rev., 217, 73

O’Shea, E., Muglach, K., & Fleck, B. 2002, A&A, 387, 642

Priest, E. 2014, Magnetohydrodynamics of the Sun (Cambridge University Press)

Reznikova, V. E., Shibasaki, K., Sych, R. A., & Nakariakov, V. M. 2012, ApJ, 746, 119

Roberts, B. 1981, Sol. Phys., 69, 39

Roberts, B. 2006, Philosophical Transactions of the Royal Society of London Series A, 364, 447

Roberts, B. 2019, MHD waves in the solar atmosphere (Cambridge University Press)

Schou, J., Scherrer, P. H., Bush, R. I., et al. 2012, Sol. Phys., 275, 229

Schuck, P. W. 2006, ApJ, 646, 1358

Schunker, H., & Cally, P. S. 2006, MNRAS, 372, 551

Sharma, A., Gupta, G. R., Tripathi, D., Kashyap, V., & Pathak, A. 2017, ApJ, 850, 206

Spruit, H. C. 1982, Sol. Phys., 75, 3

Stangalini, M., Verth, G., Fedun, V., et al. 2022, Nature Communications, 13, 479

Su, J. T., Ji, K. F., Cao, W., et al. 2016, ApJ, 817, 117

Sych, R., & Nakariakov, V. M. 2014, A&A, 569, A72

Sych, R., Nakariakov, V. M., Karlicky, M., & Anfinogentov, S. 2009, A&A, 505, 791

Tian, H., DeLuca, E., Reeves, K. K., et al. 2014, ApJ, 786, 137

Ulrich, R. K. 1970, ApJ, 162, 993

Wu, W., Sych, R., Chen, J., & Su, J.-T. 2021, Research in Astronomy and Astrophysics, 21, 126

Yurchyshyn, V., Abramenko, V., & Kilcik, A. 2015, ApJ, 798, 136

Zhao, J., Chen, R., Hartlep, T., & Kosovichev, A. G. 2015, ApJL, 809, L15

Zhao, J., & Chou, D.-Y. 2013, Sol. Phys., 287, 149

Zhugzhda, I. D., & Dzhalilov, N. S. 1984, A&A, 132, 45

Zirin, H., & Stein, A. 1972, ApJL, 178, L85

# 요약

암부 진동은 흑점의 안부에서 보이는 가장 눈에 띄는 활동 현상이다. 암부 진동은 음속으로 광구에서 코로나까지 자기장을 따라서 전파하는 느린 자기음파 (slow magnetoacoustic wave) 와 연관된다. 흥미롭게도, 최근 관측 연구는 이 파동이 복잡한 형태의 수평 양상을 가지고 자기장을 가로질러 전파하는 것 처럼 보이는 것을 보고하였다. 이러한 진동 양상의 연구는 암부진동의 본성과 기원을 알려줄 뿐만 아니라 파동이 원천 지역부터 채층 이상의 상층 대기까지 어떻게 전파되는지에 대한 정보를 알려줄 수 있기 때문에 중요하다. 게다가, 진동 양상과 파동은 원천 지역의 대기 조건을 유추하는데 유용한데 파동이 지나온 매질의 정보를 가지고 전달되기 때문이다. 암부 진동 양상의 본성을 이해하기 위한 여러 노력에도 불구하고, 아직까지 미제로 남아있다. 본 학위 논문에서 우리는 구디 태양 망원경 (Goode Solar Telescope)의 고속영상태양분광기 (Fast Imaging Solar Spectrograph)와 태양 활동 관측위성 (Solar Dynamics Observatory, SDO)의 대기 영상 관측기 (Atmospheric Imaging Assembly, AIA) 를 통해 얻은 흑점 암부에서 관측된 진동 양상의 본성을 이해할 수 있는 이론 모형을 고안하였다.

먼저, 우리는 관측된 나산형 파동 양상 (spiral-shaped wave pattern, SWP)을 꼬이지 않은 자속관의 흑점 표면 아래에서 발생한 느린 자기음파의 축대칭성 모드와 비축대칭성 모드의 중첩으로써 해석하는 이론 모형을 제안하였다. 우리는 모형을 미소흑점 (pore)에서 도플러 시선속도로 관측한 나선팔이 각각 한 개 그리고 두 개인 SWP 에 대해 적용하였다. 시선속도진동의 주기는 약 160 초 이고 5 분간 지속되었다. 제안된 모형에 따르면 나선팔 양상은 미소흑점 표면에서 1600 km 깊이에서 발진된 0 이 아닌 방위각 모드에 의해 만들어진다. 관측된 나선팔이 하나인 SWP는 자속관에서의 소시지 (sausage) 모드와 킨크 (kink) 모드에 의해 형성되고, 나선팔이 두개인 SWP는 소시지 모드와 플루팅 (flutting) 모드에 의해 형성된다.

둘 째로 우리는 SDO/AIA 304 Å 를 이용하여 SWP의 관측적 특성을 분석하였다. 2013 년부터 2018 년까지 태양 중심에서 두 시간 동안 관측된 496 개의 흑점을 조사하였다. 이 중 우리는 140 개의 흑점에서 241 개의 SWP를 찾았고 이때 발견율은 시간당

0.24 개이다; 192 개는 나선팔이 하나인 SWP, 48 개는 나선팔이 두 개인 SWP, 한 개는 나선팔이 세 개인 경우 이다. SWP의 수명은 780±250 초이고 진동 주기는 149±35 초로 일차원적인 암부진동의 결과와 유사하다. 나선팔이 한 개인 SWP의 겉보기 회전 주기는 183±72 초이고 나선팔이 두 개인 SWP는 317±132 초이다. 나선형 파동 양상의 관측적 특성은 반구, 위도 그리고 흑점 크기와 무관하다. SWP가 내부에서의 국부적인 무작위 사건 (event)에 의해 비롯된다고 가정하고 아이코날 (eikonal) 방법을 통해 계산하면, 대부분의 나선팔은 2 Mm 에서 10 Mm 사이의 표면 아래 깊이에서 발생하고 평균적으로 6 Mm 깊이에서 발생한다.

셋 째로 우리는 광구아래층 (subphotosphere)에서의 빠른 자기음파의 공명 모형을 이용하여 관측된 흑점 진동 양상의 시간 변화를 성공적으로 재현했다. 빠른 실체파 (body wave)의 절단 파수 때문에 오직 몇개의 작은 차수 모드만이 미소흑점 같은 작은 규모의 자속관에 갖히게 된다. 빠른 자기음파에서 느린 파동으로의 모드 변환 (mode conversion)에 의해서 광구아래층의 빠른 자기음파의 공명파의 상속된 양상이 채층의 느린 자기음파 양상으로써 관측될 수 있다. 이 모형은 본 학위논문에서 가장 중요한 성과이다. 이 연구는 우리가 관측할 수 있는 채층 진동 양상을 통해서 관측할 수 없는 대기 조건을 유추할 수 있다는 점에서 흑점에서의 광구 아래층의 지진학의 해결의 빛을 던지는데 있다.

우리의 이러한 접근 방식은 암부 진동의 본성과 기원에 대한 새로운 통찰을 제공한다. 이와 더불어 우리의 결과는 암부 진동 그 자체 뿐만 아니라 흑점 진동을 발생시키는 섭동과 흑점 표면 아래 내부 구조를 이해하는데 기여할 것이다.

**주요어:** 흑점; 자기유체역학; 태양 진동; 태양 대기; 태양 채층

**학 번:** 2016-20325

# Acknowledgement

I greatly appreciate all the support provided to me during my thesis work.

From 2016 to 2018, I was supported by the interdisciplinary program in space system. Chatper 2 was supported by the National Research Foundation of Korea (NRF-2017R1A2B4004466). Chapter 3 was supported by the National Research Foundation of Korea (RS-2023-00208117). Chapter **??** was supported by the National Research Foundation of Korea (RS-2023-00208117). My work has been based on the data taken by the FISS on the GST at Big Bear Solar Observatory (BBSO) and the data from the Solar Dynamics Observatory (SDO). BBSO operation is supported by NJIT, US NSF AGS-1821294 grant. GST operation is partly supported by the Korea Astronomy and Space Science Institute and Seoul National University.

‘’

# 감사의 글

한 사람이 어려서 부터 하고 싶었던 일을 업으로 삼고 끝까지 나아가는 것이 쉬운 일이 아닌데, 큰 어려움 없이 이렇게 졸업하게 되어서 감사합니다. 한 편으로는 운이 좋았고 다른 한 편으로는 주변의 많은 도움 덕분에 학위과정을 즐겁고 무난하게 끝마치게 되었습니다. 여기서는 저에게 도움과 격려를 주신 분들께 감사한 마음을 전달하고자 합니다.

먼저 학부생 인턴 때 부터 저를 지도해주신 채종철 교수님께 감사드립니다. 학부생 인턴인데도 불구하고 매주 개별 면담을 통해 직접 이론적인 설명과 프로그램을 알려주셔서 더 쉽고 재밌게 태양 연구에 접할 수 있었습니다. 대학원 입학하고 3 년간 이렇다할 연구성과를 보여드리지 못했는데도 격려해주시고 응원해주신 덕분에 포기하지 않고 연구할 수 있었습니다. 연구에 있어서도 제가 잘 못 이해한 부분이 있거나 하면 친절하게 여러 번 설명해주시고 예시를 들어주셔서 어려운 개념을 이해하는데 큰 도움이 되었습니다. 졸업하는 해에는 시도 때도 없이 교수님을 찾아뵙고 시간을 많이 뺏었는데도 교수님께서 항상 웃는 얼굴로 반겨주시고 칭찬해주셔서 연구를 재밌게 임할 수 있었습니다. 제가 교수님을 만나뵙고 재밌게 태양 연구를 할 수 있던 것이 제게 주어진 가장 큰 행운이 아닐까 싶습니다.

제 박사학위논문 심사를 맡아주신 박용선 교수님, 김웅태 교수님, 최광선 교수님, 임은경 박사님께 감사드립니다. 흔쾌히 학위 심사를 승낙해주시고 바쁘신 시간을 내주신 덕분에 제가 박사로써 발걸음을 뗄 수 있게 되었습니다. 심사 중에 주신 조언과 질문을 바탕으로 연구를 발전시킬 수 있었고, 질문 주신 내용을 토대로 앞으로 박사후 연구원 과정 때 흑점 연구 뿐만 아니라 다양한 대상에서 주제를 확장시켜 연구해볼 생각입니다.

제 첫 연구주제의 공저자로 참여해주신 Nakariakov 교수님께도 감사의 말씀을 전합니다. 경희대학교 방문 일정 중 시간을 내시어 제 연구에 조언을 주셔서 첫 논문의 내용을 보강하여 발전시킬 수 있었습니다. 또한, 그때 주신 조언을 계기로 주제를 확장시켜 이렇게 졸업할 수 있게 되었습니다.

제 연구 주제의 공저자로 참여해 준 선후배님들께도 감사의 인사를 전합니다. 가장 먼저 감사를 드리고 싶은 분은 조규현 박사님입니다. 제 첫 번째 주제의 해석 모형은 조규현 박사님이 제안한 모형을 기반으로 만들었었고 세 번째 주제 역시 박사님이 제안하신 공명을 고려하여서 이토록 연구를 발전시킬 수 있었습니다. 특히, 미국이라 새벽시간에 제가 질문을 드린 건데도 다양한 해석 방식과 연구 주제를 논의해주셔서 앞으로도 재미나게 연구를 할 수 있을 것 같습니다. 이후에도 같이 공동 연구를 수행하기를 희망합니다. 심사위원이자 공저자로 참여해 주신 임박사님께도 감사드립니다. 제가 급하게 논문을 보내드렸는데 새벽까지 읽어보시고 조언을 주신 덕분에 논문이 조금 더 잘 다듬어졌습니다. 이외에도 항상 밝게 맞아주고 같이 논의한 한나 누나, 제 초창기 아이디어를 가장 열심히 들어주고 공감해준 겨레형, 그리고 마치 자기 연구인 듯 열정적으로 참여한 수상이, 또 바쁜데도 불구하고 시간내서 통계자료 처리를 도와준 주연이에게 감사의 마음을 전합니다. 공저자로 참여하지 않았지만 재밌게 같이 이야기하고 연구 내용을 공유했던 이경선 박사님, 항상 친절하게 대해주신 정혜원 박사님, 연구외에 모르는게 없던 민주형, 항상 씩씩하고 쾌활했던 다나, 학부생 연구원으로 열정적로 참여했던 병하와 유정이, 실로스탯 운용에 참여한 현용이, 그리고 새롭게 팀에 들어와서 재밌게 연구를 시작한 민재와 영훈이에게도 감사합니다. 학부 연구생 때 지원과 많은 도움을 주신 임명신 교수님 감사드립니다.

사회에서 만난 선후배 박사님들과 천문연 박사님들께도 감사합니다. 가장 먼저 천문연에서 저를 가장 많이 챙겨준 희수 형과 형수님께 감사드립니다. 주말에도 혼자서 밥먹을까봐 챙겨주시고, 평일에도 대전 방방곳곳에 데리고 가서 맛집 탐방과 대청호수에 등에 데려가주셔서 덕분에 외롭지 않게 재미나게 보낼 수 있었습니다. 같이 일하면서 많이 싸우기도 하고 서로 티격태격하긴 했지만 덕분에 조금 더 학자로써 그리고 한명의 어른으로 성장할 수 있는 계기가 되었습니다. 마찬가지로 동욱이 형도 같이 일하면서 많이 티격태격하기도 했지만, 저랑 같이 놀아주시고 신경써주셔서 감사합니다. 늦게까지 같이 일하면서 같이 야식도 많이 먹고 차로 저희 집까지 데려다 주셨어서 재밌게 시간을 보낼 수 있었습니다. 특히 두 분이 제 얘기를 많이 공감해주신 덕분에 스트레스도 많이 풀리고 힘내서 일할 수 있어서 좋았습니다. 먼저 나갔지만 함께 코로나그래프

개발과 환경시험 등 여러 일을 같이한 김진현 선생님께도 감사드립니다. 정말 짜증도 많이 내고 했었는데 위트있게 받아주시고 같이 힘써주셔서 덕분에 일을 잘 마무리할 수 있었습니다. 코로나그래프 개발에서 시스템 엔지니어로서 개발 과정을 이끌어주신 최성환 박사님 그리고 프로젝트 책임자로서 전반적으로 이끌어주신 김연한 박사님께도 감사드립니다. 논의를 통해 기기 개발에 있어서 많은 것을 배울 수 있었고, 고군분투하는 저희를 위해서 격려와 지원을 아끼지 않으신 덕분에 힘을 낼 수 있었습니다. 그리고, 연구 관련 조언을 해주신 조경석 박사님, 환경시험 관련에서 많은 조언을 주신 손종대 박사님, 광학 기기에 관련하여 조언을 아끼지 않으신 김지헌 박사님, 프로그램 개발에 있어 도움을 주신 박종엽 박사님과 백지혜 선생님, 열진공 시험과 진동 시험 등 환경시험에 많은 도움을 주신 문봉곤 박사님, 방사선 시험을 혼자간다고 하니 도와주시겠다고 같이 참여해주신 남욱원 박사님, 카메라 개발과 회로 관련하여 항상 도움을 주신 김정웅 사장님과 아이트릭스 직원분들 (조병경, 이다교, 조인혁, 이용기, 박시열, 주형우), 카메라 소프트웨어 개발과 환경시험 보조물을 개발에 도움을 주신 앤트브릿지 정광희 사장님, 진현씨가 나가고 특성측정과 여러 일로 도움을 준 방병채 선생님과, 그리고 환경시험에 도움을 준 천문연 박사님들 (김연한, 최성환, 남욱원, 문봉곤, 김록순, 장비호, 봉수찬, 김수진, 서정준, 이재옥, 이환희, 김진현, 방병채, 한정열)과 전문연구요원 이찬행 선생님 모두에게 감사드립니다. 지금은 경희대에 계시지만 혼자 천문연에 내려온 제가 초반에 적응하기 힘들까봐 많이 도와주시고 격려해주신 장수정 박사님, 감사합니다. 제가 빅베어 천문대에 관측가거나 수리하러 갔을 때도 항상 시간 내주셔서 확인해주시고 신경써주신 안광수 박사님께도 감사드립니다. 천문연에서 같이 놀고 재미난 이야기 해주신 권윤영 박사님, 김정헌 박사님, 감호식 박사님, 박은수 박사님, 천문연에서 또래로 같이 놀아준 곽재영 선생님과 이재욱 선생님, 송호섭 선생님께도 감사드립니다. 전문연 관련해서 많이 조언해주고 응원해준 양하늘 박사님 덕분에 잘 끝마칠 수 있었습니다. 행정 업무로 항상 도와주신 윤누리 선생님 감사합니다.

대학 동기와 선후배 덕분에 즐거운 대학 및 대학원 생활을 하였습니다. 항상 같이 밥먹고 이야기 하며 재미난 일 뿐만 아니라 불평불만을 같이 공유하며 대학원 생활을 재미나게 보낸 건우, 덕분에 즐거웠다. 항상 저를 생각하고 아껴준 창수형, 하늘이 형이

랑 같이 항상 격려해고 응원해준 지수 누나, 대학 생활부터 같이 고군분투한 상혁이형, 본 받을게 많은 윤수, 항상 재밌는 성용이, 정 많은 소피아 누나, 잘생긴 민철이형과 그 옆의 범후씨, 항상 신나는 나은이, 말장난 하고 노는게 재밌었던 수현이, 똑똑한 호진이형, 누구보다 열심히인 정환이형, 인턴 생활을 도와준 용정이 형과 윤찬이형, 민희누나, 전이슬 박사님, 감사합니다. 그리고, 행정실 노조교님 덕분에 행정관련 도움을 많이 받고 학부부터 대학원까지 순탄하게 지낼 수 있었습니다.

고등학교 친구들한테도 고마움을 전합니다. 천문연에 있을 때도 굳이 먼 곳까지 와서 전문연 전역을 축하해준 호영이, 건태, 은빈, 주국아 고마워. 특히 호영이는 박사 졸업한다고 하니 바쁠텐데도 격려차 학교까지 들러주어 고마워. 그리고 함께 같이 놀아준 과특 친구들 재직이, 진이, 찬빈이, 효정이, 소연이, 유정이도 고맙고 시간내서 같이 모이면 좋겠다.

끝으로 저를 가장 많이 응원해주고 지지해준 가족에게 감사드립니다. 격려하고 지지해준 우리 아빠, 항상 내 몸부터 생각해주고 아껴준 사랑하는 우리 엄마, 그리고 티격태격하지만 날 먼저 위해주는 우리 형, 감사하고 사랑합니다. 그리고 절 응원해준 친척분들께도 감사하다는 말 전합니다.

끝으로 제가 실수로 누락했을 저를 응원해주신 많은 분들께도 감사드립니다.

2023년 8월
강 주 형 올림